

Dense Associative Memories with Analog Circuits

Marc Gong Bacvanski¹, Xincheng You², John Hopfield³, and Dmitry Krotov⁴

¹MIT

²Independent Researcher

³Princeton University

⁴IBM Research

December 16 2025

Abstract: The increasing computational demands of modern AI systems have exposed fundamental limitations of digital hardware, driving interest in alternative paradigms for efficient large-scale inference. Dense Associative Memory (DenseAM) is a family of models that offers a flexible framework for representing many contemporary neural architectures, such as transformers and diffusion models, by casting them as dynamical systems evolving on an energy landscape. In this work, we propose a general method for building analog accelerators for DenseAMs and implementing them using electronic RC circuits, crossbar arrays, and amplifiers. We find that our analog DenseAM hardware performs inference in *constant* time independent of model size. This result highlights an asymptotic advantage of analog DenseAMs over digital numerical solvers that scale at least linearly with the model size. We consider three settings of progressively increasing complexity: XOR, the Hamming (7,4) code, and a simple language model defined on binary variables. We propose analog implementations of these three models and analyze the scaling of inference time, energy consumption, and hardware. Finally, we estimate lower bounds on the achievable time constants imposed by amplifier specifications, suggesting that even conservative existing analog technology can enable inference times on the order of tens to hundreds of nanoseconds. By harnessing the intrinsic parallelism and continuous-time operation of analog circuits, our DenseAM-based accelerator design offers a new avenue for fast and scalable AI hardware.

1 Introduction

The unprecedented growth of artificial intelligence (AI) has driven demand for increasingly large and powerful models. At present, the field of generative AI is primarily driven by two settings: autoregressive transformers [1] and diffusion models [2]. While these settings have demonstrated remarkable capabilities, they do so at a substantial computational cost. Their current implementations utilize digital computation, which faces fundamental challenges in energy efficiency, scalability, and latency, especially as model sizes and deployment demands continue to grow [3, 4, 5]. These limitations have prompted interest in alternative computational paradigms that can efficiently handle the demands of modern AI workloads [6].

Dense Associative Memories (DenseAMs) [7, 8], a promising class of AI models which generalize Hopfield networks [9], offer a new angle for tackling these problems. Unlike conventional feed-forward models, DenseAM inference can be defined through the temporal evolution of a state vector that is governed by a system of differential equations [10]. The state vector can be thought of as a particle exploring the surface of a high-dimensional energy landscape, which is the Lyapunov function of these dynamical equations. DenseAMs have been demonstrated to be flexible and expressive computational frameworks, capable of representing many primitives of modern AI architectures, such as attention mechanism [11], transformers [12], and diffusion models [13, 14, 15]. Furthermore, DenseAMs are error-correcting systems [16], a property ensuring that small perturbations of the desired temporal evolution of the state vector are corrected away by the dynamics of the network itself, rather than accumulated in time. Finally, DenseAMs are asymptotically stable—during the course of temporal evolution the computation happens during a finite transient period of time, which is followed by a steady state of

Code available at <https://github.com/mbacvanski/AnalogET>.

neural activities. This asymptotic stabilization of dynamical trajectories removes the requirement to read out the “answer” to the computation problem at a precise moment of time, making DenseAMs robust to several classes of hardware imperfections. The confluence of the above properties makes DenseAMs appealing networks for analog hardware implementations that, on the one hand, are grounded in the physics of stable error-correcting dynamical systems and, on the other hand, are capable of representing computation in state-of-the-art AI networks.

In 1989, Hopfield argued that analog neural hardware can exceed the efficiency of digital implementations when the device physics directly instantiate the computational dynamics of the model itself [17]. Here, we revisit this idea with DenseAM models: we propose an analog circuit-based hardware accelerator design whose dynamics directly realize those of the DenseAM. We find that analog DenseAM hardware enables constant-time inference independent of model size, which is in stark contrast to GPU solvers and digital implementations. This intrinsic property makes DenseAM a natural fit for analog AI accelerators, and it highlights our circuit architecture as a viable hardware path to realize them. Using component specifications already demonstrated in fabricated devices, analog DenseAM hardware may achieve inference times on the order of tens to hundreds of nanoseconds, several orders of magnitude faster than digital systems.

By leveraging the natural dynamics of analog systems, this work establishes a new design of fast and scalable AI accelerators. The framework of DenseAMs and their efficient analog hardware implementations suggest a pathway for fundamentally redesigning the hardware-software interface for AI, enabling a new paradigm for fast, energy-efficient, and scalable computation.

2 Dense Associative Memory basics

The DenseAM framework [10, 18] provides a model that has straightforward neuronal dynamics, yet is surprisingly expressive in its ability to represent AI models including transformer attention, diffusion models, and associative memories. In its simplest form it is defined by two sets of neurons (typically called visible and hidden neurons) and a system of coupled non-linear differential equations governing their behavior, see Figure 1. The visible neurons are characterized by their internal states v_i and their outputs g_i , index $i = 1 \dots N_v$; while the hidden neurons have internal states h_μ and outputs f_μ , index $\mu = 1 \dots N_h$. From the AI perspective, one can think about internal state of the neuron as a pre-activation of that neuron, and the output as a post-activation, which is obtained by applying an activation function to the pre-activation. From the biological perspective, one can think about the internal state of the neuron as a membrane voltage potential, and the output of that neuron as an axonal output, or a firing rate of that neuron. This framework admits both neuron-wise activation functions ($g_i = g(v_i)$, where $g(\cdot)$ is some continuous function, e.g., a ReLU), and collective activation functions such as softmax or layer normalization, which depend on the states of multiple neurons.

The network parameters are stored in the synaptic weights $\xi \in \mathbb{R}^{N_h \times N_v}$, whose matrix elements denoted by $\xi_{\mu i}$ can be either hand-engineered or learned. The time decay constants for the two groups of neurons are τ_v and τ_h . With these conventions, the temporal evolution of the two groups of neurons can be expressed as

$$\begin{cases} \tau_v \frac{dv_i}{dt} = \sum_{\mu=1}^{N_h} \xi_{\mu i} f_\mu + a_i - v_i \\ \tau_h \frac{dh_\mu}{dt} = \sum_{i=1}^{N_v} \xi_{\mu i} g_i + b_\mu - h_\mu \end{cases} \quad (1)$$

This forms a bipartite graph of neuronal connections, where the state of the hidden neurons is updated by the state of the visible neurons, and vice versa. Importantly, the same matrix ξ appears in both equations, once as ξ and again as ξ^\top . Although this is sometimes described as using “symmetric” weights, ξ is not assumed to be symmetric in the linear-algebraic sense; it is simply the same matrix used in both directions. Finally, a_i and b_μ denote biases, which are additional weights of the system and whose values may be hard-coded or learned depending on the application.

The most important aspect of this model is the existence of a global energy function (Lyapunov function) that describes neuronal dynamics. To demonstrate this, it is most convenient to use the Lagrangian formalism [10, 18, 16]. Each set of neurons is defined through a Lagrangian function of their internal states. The activation functions are defined as partial derivatives of that Lagrangian with respect to internal states. The total energy is the sum of energies of each set of neurons, plus the interaction

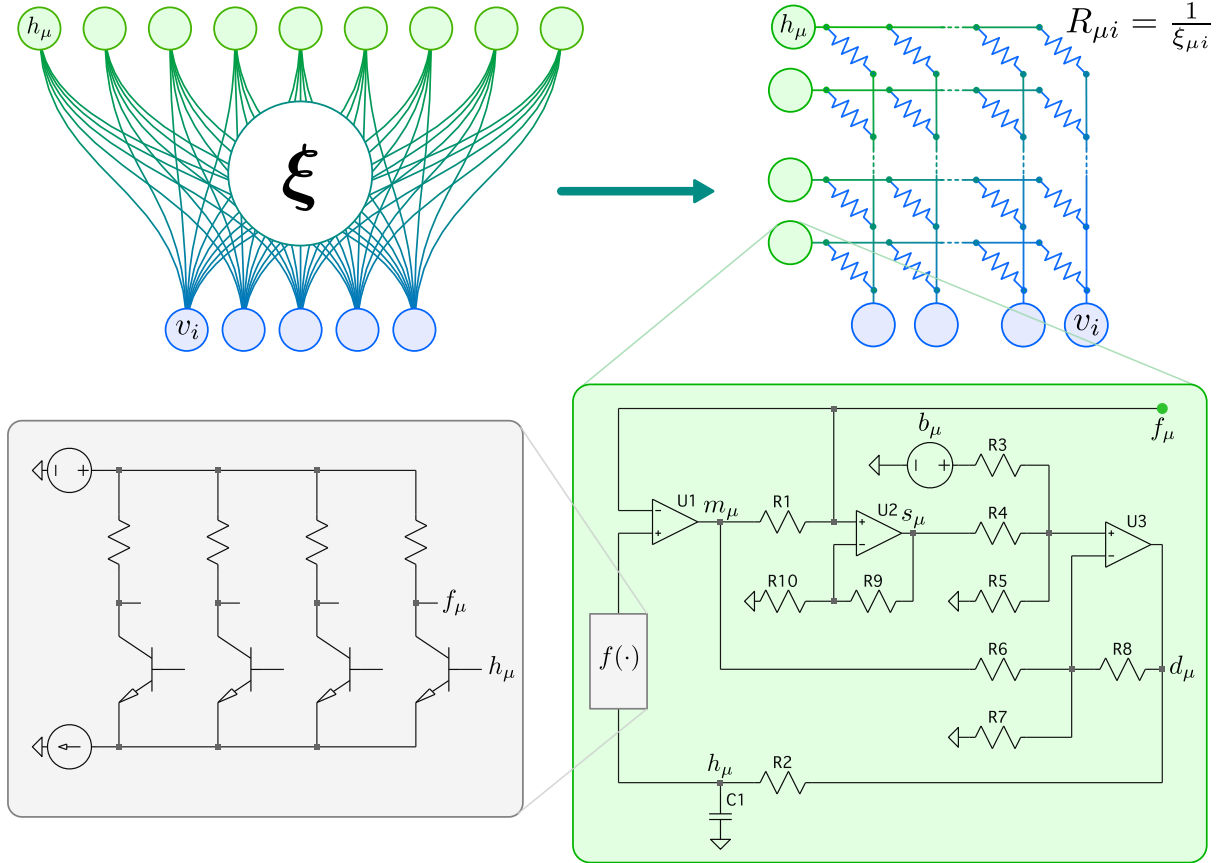


Figure 1: **Top left:** Bipartite neural network formulation, where hidden neurons h_μ and visible neurons v_i are connected via symmetric synaptic weights ξ . **Top right:** Circuit realization of symmetric weight matrix via resistive crossbar array. Each crosspoint encodes a weight $\xi_{\mu i}$ by its resistance $R_{\mu i} = 1/\xi_{\mu i}$. **Lower right:** Circuit schematic of a single hidden neuron. It drives its row of the crossbar array with a voltage according to its activation f_μ , and its internal dynamics are driven by the incoming current flowing into it from the crossbar array. **Lower left:** Softmax activation function built from bipolar junction transistors (some components not shown).

energy. The energy of each set of neurons is a Legendre transformation of the corresponding Lagrangian (plus the term proportional to the bias). Thus, the global energy of Equation 1 is given by

$$E = \underbrace{\left(\sum_{i=1}^{N_v} g_i(v_i - a_i) - \mathcal{L}_v \right)}_{\text{energy of visible neurons}} + \underbrace{\left(\sum_{\mu=1}^{N_h} f_\mu(h_\mu - b_\mu) - \mathcal{L}_h \right)}_{\text{energy of hidden neurons}} - \underbrace{\sum_{\mu=1}^{N_h} \sum_{i=1}^{N_v} f_\mu \xi_{\mu i} g_i}_{\text{interaction energy}} \quad (2)$$

where the activation functions are defined as partial derivatives of the Lagrangians

$$g_i = \frac{\partial \mathcal{L}_v}{\partial v_i}, \quad f_\mu = \frac{\partial \mathcal{L}_h}{\partial h_\mu}$$

For convex Lagrangians this global energy decreases with time on the dynamical trajectories of Equation 1. If, additionally, the activation functions (and corresponding Lagrangians) are chosen in such a way that this energy is bounded from below, the dynamical trajectories are guaranteed to arrive at a stable fixed point of activations. The dynamical equations typically have many asymptotic fixed points, which correspond to local minima of the energy function in Equation 2. Both properties above (convexity of Lagrangians and lower-bounded energy) are satisfied for all settings studied in this paper. By picking different nonlinear activation functions (or corresponding Lagrangians), this system yields a variety of models that can describe associative memory, softmax attention, and other commonly used settings in AI [10, 11, 18, 19, 20].

A particularly relevant example for modern sequence modeling is the Energy Transformer (ET) [12], which reformulates transformer's inference pass as a gradient flow on an energy function defined over the

set of tokens. The ET block contains two contributions to the energy function: attention energy and the Hopfield network. The energy attention module routes the information between the tokens, while the Hopfield module aligns the tokens with the manifold of token embeddings. In our implementation, the context tokens act as a set of dynamically instantiated memories that interact with the predicted token through a DenseAM-like energy. In section 6 we exploit this connection to construct an Analog Energy Transformer (Analog ET) whose continuous-time dynamics are implemented directly in hardware using our DenseAM circuit primitives.

3 Related work

Early analog implementations of associative memories focused on the classical Hopfield network. Foundational designs, such as continuous-time analog circuits [21, 22] and later demonstrations using amorphous-silicon resistors [23], memristive devices [24, 25], and phase-change memories [26], targeted the quadratic Hopfield energy function. These works emphasize device engineering and memory-cell design rather than system-level dynamics, and inherit the limited storage capacity and representational power of traditional Hopfield networks. That line of research is largely concerned with how to fabricate programmable resistance elements themselves; our work assumes programmable conductances as a given primitive and focuses on the continuous-time dynamics that operate on top of them. Our work also differs from these works by addressing DenseAMs with higher-order energy functions and continuous-valued states.

Another direction is the use of cavity-QED systems for associative memory. Marsh et al. [27] analyze a confocal cavity implementation of a quadratic Hopfield network and show that the cavity dynamics induce a descent-like relaxation rule on spin states. Their model remains restricted to quadratic energies and binary spins, and operates in a cryogenic, cavity-QED setting. Our work instead targets higher-order DenseAMs with continuous states, and emphasizes scalable, room-temperature analog microelectronics with explicit hardware-aware dynamical analysis.

More recent physical implementations move beyond purely quadratic energies. Musa et al. [28] propose a free-space optical realization of the higher-order DenseAM energy. Their system constructs a static physical representation of the energy landscape, but inference relies on an external digital controller that performs iterative spin-flip updates. Thus, the hardware computes energies, while the optimization dynamics remain digital. In contrast, our analog microelectronic architecture embeds the gradient flow itself into hardware: inference is performed by a single continuous-time evolution rather than by discrete digital updates.

4 DenseAM circuit design

Here, we introduce a novel architecture for a class of analog electronic hardware accelerators that models Equation 1’s system of nonlinear differential equations using time evolution. Our DenseAM design shown in Figure 1 is comprised of two sets of neurons that interact through a resistive crossbar array. The resistive crossbar array turns voltage differences between neurons into currents flowing between the neurons according to synaptic weights, and each neuron’s internal circuitry converts those currents into dynamics that reproduce Equation 1.

Resistive weights as a crossbar array. The crossbar array construction is a canonical design of matrix-vector multiplication using analog electronics [17, 29], and is a natural fit for the weight matrix ξ in our model. Traditionally, each crosspoint between a row and column line is connected by a resistor (often memristors, RRAM, or other analog memories that produce resistances), a vector of input voltages is applied at row lines, and the column lines are held at ground typically via a transimpedance amplifier. By Ohm’s law, each resistive crosspoint produces a current that multiplies the row’s input voltage by the inverse of the resistance. Because currents add along each column line, the total current output at a column is the inner product between the vector of input voltages and the column’s conductance vector. Thus, the array as a whole implements a parallel analog matrix multiplication of the form $I_{\text{out}} = GV_{\text{in}}$, where G is the matrix of conductances (inverse of resistances).

Unlike a traditional crossbar array whose rows are driven at a fixed voltage and whose columns are held at ground, our DenseAM circuit design uses each weight bidirectionally, exactly representing the bidirectional connections between visible and hidden neurons. As a result, the current flowing into each neuron corresponds to the weighted sum of the differences between visible and hidden neuron activations. For example, for hidden neuron μ , this current is $\sum_i \xi_{\mu i} (g_i - f_\mu)$. This construction enables

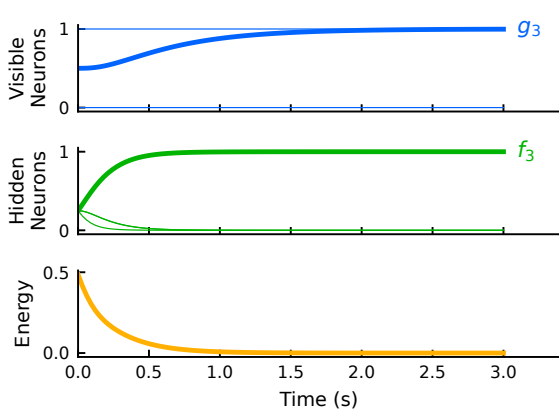


Figure 2: Solving XOR with a DenseAM. Visible neuron $g_3 = v_3$ serves as the output, while the two input neurons (unlabeled, thin lines) are clamped at 1 and 0 for True and False. Output v_3 is initialized at 0.5 and converges to a positive prediction of 1. The activation of the hidden neuron f_3 for the truth-table row (1, 0, 1) becomes highly activated, with others (fine lines) are suppressed by softmax. Energy (2), or equivalently (5), decreases monotonically along the inference trajectory.

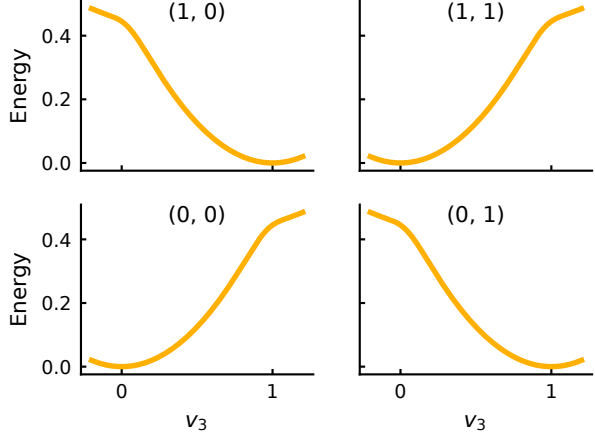


Figure 3: XOR energy landscape of neuron v_3 under different settings of visible input neurons v_1 and v_2 . Minima in the energy function correspond to stationary points of the dynamics. Gradient flow dynamics bring v_3 to these attractor points, resulting in correct XOR outputs.

weight symmetry to be enforced by hardware sharing: both forward and reverse weights are realized by the same resistive elements. Importantly, as long as weights are represented as conductances, they must be non-negative.

Design of a single neuron. Each neuron in the circuit computes its dynamics by integrating the currents it receives from the crossbar array, which represent weighted differences between its own activation and those of connected neurons. Considering a hidden neuron (the design for visible neurons is symmetric by design), the neuron’s internal voltage h_μ is stored on capacitor C_1 and evolves in continuous time, while the neuron’s activation f_μ is obtained by passing h_μ through a nonlinear function (e.g. ReLU or softmax).

The current flowing into hidden neuron μ is produced by its interaction with all visible neurons via the synaptic weights $\xi_{\mu i}$ for $i = 1, \dots, N_v$. Specifically, this is as a weighted sum of the differences between neuron activations: $\sum_i \xi_{\mu i} (g_i - f_\mu)$. Inside each neuron, a “self” path scales f_μ to produce the voltage $s_\mu = f_\mu \sum_i \xi_{\mu i}$. This term is added to the value of the incoming current so that the $-f_\mu \sum_i \xi_{\mu i}$ term is cancelled inside each neuron. As a result, the hidden state, represented as the voltage across capacitor C_1 , integrates only the desired weighted input plus any external stimulus b_μ . Its dynamics reduce to the canonical DenseAM form with a time constant of $R_2 C_1$:

$$R_2 C_1 \frac{dh_\mu}{dt} = \sum_{i=1}^{N_v} \xi_{\mu i} g_i + b_\mu - h_\mu \quad (3)$$

Elementwise (or vectorized) nonlinearities then produce activations $g_i = g(v_i)$ and $f_\mu = f(h_\mu)$ (e.g., ReLU, softmax) across the visible and hidden neurons. See Appendix A for the full circuit derivation.

5 Analog DenseAM Examples

We begin by studying two examples of the proposed design: the XOR task, and the (7,4) error-correcting Hamming code.

5.1 XOR

The XOR problem is a canonical test for nonlinear representation and inference, as it cannot be solved by any linear model. We show a minimal DenseAM model for the XOR task, illustrating how energy-based dynamics can solve this simple task with a continuous-time analog system. The network consists of $N_v = 3$ visible neurons, and $N_h = 4$ hidden neurons. At $t = 0$ visible neurons v_1 and v_2 are initialized at their input values corresponding to the input bits. The last visible neuron v_3 is initialized at $v_3 = 0.5$. The hidden neurons are initialized at zero. The two input visible neurons remain clamped during the dynamics, while the third output visible neuron and the hidden neurons evolve in time according to (1). Each row of the memory matrix ξ corresponds to a row of the XOR truth table. The visible neurons use an identity activation function where $g_i = v_i$, and the hidden neurons use a softmax activation. The biases are set as

$$a_i = 0, \quad b_\mu = -\frac{1}{2} \sum_{i=1}^{N_v} (\xi_{\mu i})^2$$

Figure 2 shows the temporal evolution of visible and hidden neuron activations, as well as the total energy, during inference on the XOR input $(1, 0)$. The output visible neuron’s activation g_3 gradually converges to the correct prediction of 1, while the hidden neuron associated with that memory, f_3 , becomes strongly activated and the remaining hidden neurons are suppressed by the softmax nonlinearity. The system’s energy decreases monotonically throughout the trajectory and stabilizes once the network reaches its fixed-point prediction. Figure 3 depicts the system’s energy landscape as a function of output neuron v_3 for different clamped input configurations (v_1, v_2) . In each case, the energy exhibits a clear convex minimum at the correct XOR output, demonstrating that gradient flow along the energy surface drives v_3 reliably toward the correct prediction. As shown in Appendix C, we validate our circuit design and dynamics using SPICE simulation.

To analyze this DenseAM, it is instructive to consider the limit $\tau_h \rightarrow 0$. Since the second equation in (1) is linear in hidden units h_μ , they can be integrated out. With $\sum_{\mu=1}^{N_h} f_\mu = 1$, the resulting dynamics of the visible neurons can be written as

$$\tau_v \frac{dv_i}{dt} = \sum_{\mu=1}^{N_h} (\xi_{\mu i} - v_i) f_\mu \quad \text{where} \quad f_\mu = \text{softmax}\left(-\frac{\beta}{2} \sum_{i=1}^{N_v} (\xi_{\mu i} - v_i)^2\right) \quad (4)$$

The effective energy on the visible neurons can be written as

$$E^{\text{eff}}(\mathbf{v}) = -\frac{1}{\beta} \log \sum_{\mu=1}^{N_h} \exp \left[-\frac{\beta}{2} \sum_{i=1}^{N_v} (\xi_{\mu i} - v_i)^2 \right] \quad (5)$$

Intuitively, each hidden neuron computes a squared Euclidean distance between the visible state and its stored pattern ξ_μ . The softmax nonlinearity assigns higher weight to the pattern closest to the current state of the visible neurons. The resulting visible neuron dynamics are gradient flow for this effective energy. It is important to note that memories in this implementation are represented by conductances of the crossbar array, which are always positive. For this reason, matrix elements of memories $\xi_{\mu i}$ must be positive, necessitating the use of the bias terms, which are just voltage sources that can be arbitrarily signed.

While a time constant of $\tau_h = 0$ is impossible to physically construct due to finite conductances and nonzero capacitances, setting $\tau_h \ll \tau_v$ realizes the same adiabatic limit in practice. When hidden neurons evolve much faster than visible ones, they reach their steady state almost instantaneously for each configuration of visible neurons. The result is an adiabatic elimination of hidden dynamics, yielding the effective visible-only dynamics above. In practice, for the XOR task, even a relatively modest $\tau_h = \tau_v/10$ ratio yields perfect performance.

5.2 Hamming (7,4) code

The Hamming (7,4) code is an error-correcting code that encodes 4 data bits into a 7-bit codeword by adding 3 parity bits. The resulting 7-bit strings are special: only certain patterns are valid codewords, and they are spaced apart so that if a single bit is flipped, the error can be detected and corrected [30]. Table 1 lists the 16 codewords corresponding to four arbitrary data bits.

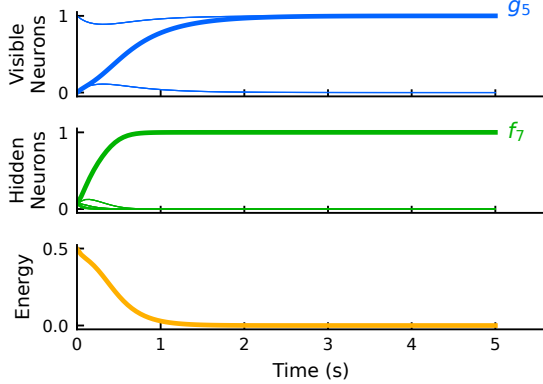


Figure 4: Correcting a bit error in a Hamming (7,4) code. Visible neuron g_5 flips indicating the bit flip error happened on the 5th codeword bit. f_7 is the hidden neuron corresponding to the memory of the correct codeword. Thin lines correspond to the other neuron activations.

Data bits ($d_1d_2d_3d_4$)	Codeword ($c_1c_2c_3c_4c_5c_6c_7$)
0000	0000000
0001	0001111
0010	0010110
0011	0011001
0100	0100101
0101	0101010
0110	0110011
0111	0111100
1000	1000011
1001	1001100
1010	1010101
1011	1011010
1100	1100110
1101	1101001
1110	1110000
1111	1111111

Table 1: Valid codewords of the Hamming(7,4) code, ordered by their 4-bit data payload.

Unlike the XOR case where the only evolving neuron is the readout bit, the Hamming (7,4) code may require flipping the value of any one of the visible neurons. During inference, the visible neurons are initialized to the corrupted 7-bit input word. All neurons are left free to evolve, and the dynamics relax the state toward the nearest stored codeword. Energy minima are located at the valid codewords, so the network converges to the correct code provided the error is within the Hamming radius of 1. Thus, the DenseAM replicates the standard decoding property of the Hamming (7,4) code: any single-bit flip is corrected automatically. Figure 4 illustrates a case where a flipped bit g_5 is restored during convergence.

The Hamming (7,4) model’s 7 visible neurons, each corresponding to a codeword bit, are connected to 16 hidden neurons, each representing one valid codeword. The weight matrix $\xi \in \{0, 1\}^{16 \times 7}$ is formed by stacking the 16 codewords as its rows. Visible neurons have the identity activation, hidden neurons use a softmax activation, and biases are chosen as in the XOR case to give the same integrated-out visible dynamics as (4).

6 Analog Energy Transformer (Analog ET) via DenseAM

Our DenseAM circuit construction can be used to build more complex energy-based models, such as the transformer-like architecture proposed in the Energy Transformer paper [12]. For causal next-token prediction with a single attention head, the Energy Transformer’s energy function can be written as the following (See Appendix J for full derivation):

$$E = \frac{1}{2} \|\mathbf{v} - \mathbf{a}\|^2 - \mathbf{v}^\top \left((\xi^{\text{attn}})^\top \mathbf{f}^{\text{attn}} + (\xi^{\text{hopf}})^\top \mathbf{f}^{\text{hopf}} \right) + (\mathbf{f}^{\text{attn}})^\top (\mathbf{h}^{\text{attn}} - \mathbf{b}) + (\mathbf{f}^{\text{hopf}})^\top (\mathbf{h}^{\text{hopf}} - \mathbf{c}) - L^{\text{attn}}(\mathbf{h}^{\text{attn}}) - L^{\text{hopf}}(\mathbf{h}^{\text{hopf}}) \quad (6)$$

with the activation functions and their Lagrangians defined as

$$f_A^{\text{attn}} = \text{softmax}(\beta \mathbf{h}^{\text{attn}})_A, \quad L^{\text{attn}}(\mathbf{h}) = \frac{1}{\beta} \log \sum_{A=1}^L e^{\beta h_A} \quad (7)$$

$$f_\mu^{\text{hopf}} = \text{ReLU}(h_\mu^{\text{hopf}}), \quad L^{\text{hopf}}(\mathbf{h}) = \frac{1}{2} \sum_{\mu=1}^M \left[\text{ReLU}(h_\mu) \right]^2 \quad (8)$$

where \mathbf{a} , \mathbf{b} , and \mathbf{c} correspond to the biases of the visible neurons, attention hidden neurons, and Hopfield network hidden neurons, respectively. The L context tokens are indexed by A , and the M hidden neurons of the Hopfield network are indexed by μ . Because the visible units use an identity activation function,

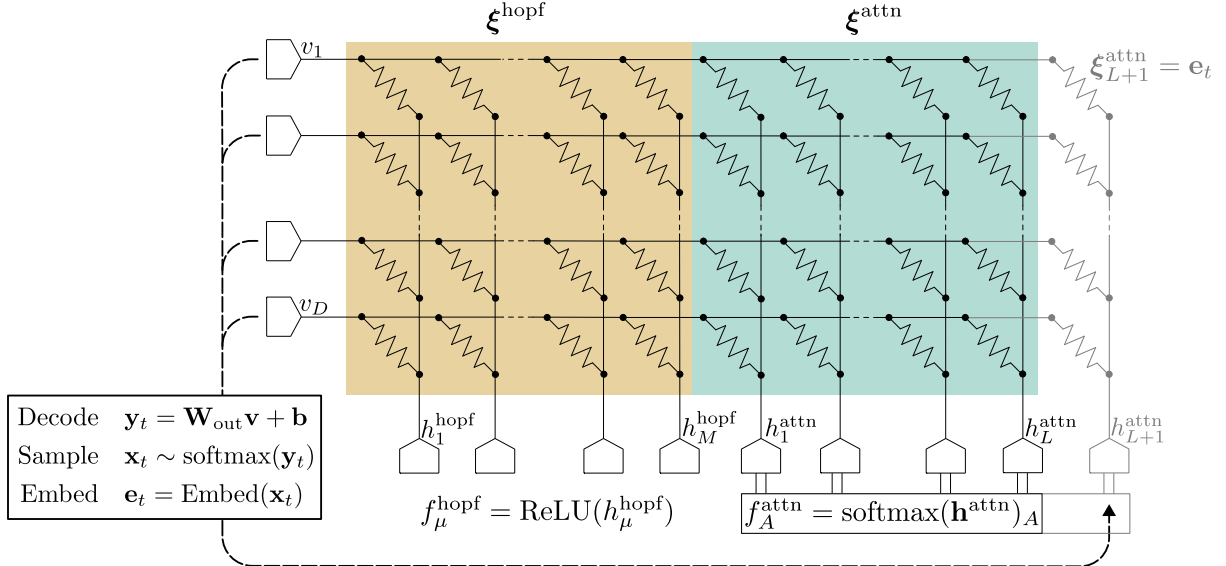


Figure 5: Analog ET circuit demonstrating the autoregressive inference procedure. A newly inferreded token is decoded, sampled, and re-embedded to obtain the weight vector ξ_{L+1}^{attn} , which is set as the weight vector for a new hidden neuron h_{L+1}^{attn} in the energy attention block (light gray on right). For this layout we have flipped the crossbar array, so that indices A and μ run horizontally and index i runs vertically.

$g_i = v_i$ using the language of Equation 1, the gradient flow of the energy yields the dynamics:

$$\tau_v \dot{\mathbf{v}} = -\frac{\partial E}{\partial \mathbf{v}} = (\xi^{\text{attn}})^T \mathbf{f}^{\text{attn}} + (\xi^{\text{hopf}})^T \mathbf{f}^{\text{hopf}} + \mathbf{a} - \mathbf{v} \quad (9)$$

$$\tau_h \dot{\mathbf{h}}^{\text{attn}} = -\frac{\partial E}{\partial \mathbf{f}^{\text{attn}}} = \xi^{\text{attn}} \mathbf{v} + \mathbf{b} - \mathbf{h}^{\text{attn}} \quad (10)$$

$$\tau_h \dot{\mathbf{h}}^{\text{hopf}} = -\frac{\partial E}{\partial \mathbf{f}^{\text{hopf}}} = \xi^{\text{hopf}} \mathbf{v} + \mathbf{c} - \mathbf{h}^{\text{hopf}} \quad (11)$$

In this formulation, \mathbf{v} represents the embedding of the output (next) token, and its evolution is driven by two terms: one term from the energy attention with weights ξ^{attn} and hidden neuron activations \mathbf{f}^{attn} , and one term from the Hopfield network with weights ξ^{hopf} and hidden neuron activations \mathbf{f}^{hopf} . The weights of the energy attention DenseAM are dependent on the context: for a token dimension D , context length L , and the task of predicting the token at index $L + 1$, the weights $\xi^{\text{attn}} \in \mathbb{R}^{L \times D}$ are generated by embedding each token of the context via a learned embedding matrix applied to each context token. In contrast, the Hopfield network weights ξ^{hopf} are learned during training and fixed at inference. The number of memories in the Hopfield network is a hyperparameter M , such that $\xi^{\text{hopf}} \in \mathbb{R}^{M \times D}$.

This system suggests a hardware implementation where \mathbf{v} interacts with two independent DenseAMs, one for the energy attention and one for the Hopfield term, which can share the same physical crossbar structure. Figure 5 shows that the circuit structure remains a crossbar array (like Figure 1), but with two distinct classes of hidden neurons. Because of the summation of currents along each row of the crossbar array, the incoming current to visible neuron v_i is the sum of contributions from the energy attention block and from the Hopfield network block. The energy attention hidden neurons \mathbf{h}^{attn} use a softmax activation function, while the Hopfield network hidden neurons \mathbf{h}^{hopf} use a ReLU activation.

6.1 Analog Energy Transformer on the parity task

We build and evaluate the Analog ET on the L -bit parity task, which can be thought of as an elementary ‘language model’: given bits $\text{bit}_1, \dots, \text{bit}_L$, predict $\text{bit}_{L+1} = (\sum_{A=1}^L \text{bit}_A) \bmod 2$. Parity is instructive because it requires a representation of a global, order- L interaction, precluding linear and shallow models from representing it efficiently. A successful model must be able to form high-order interactions in order to generalize. We formulate parity as a next-token prediction problem: given an L -bit string as context, predict its parity in the next token.

We train the Analog ET model digitally using backpropagation through time [31] implemented with Jax’s automatic differentiation. The resulting weights can be deployed onto the analog hardware; in

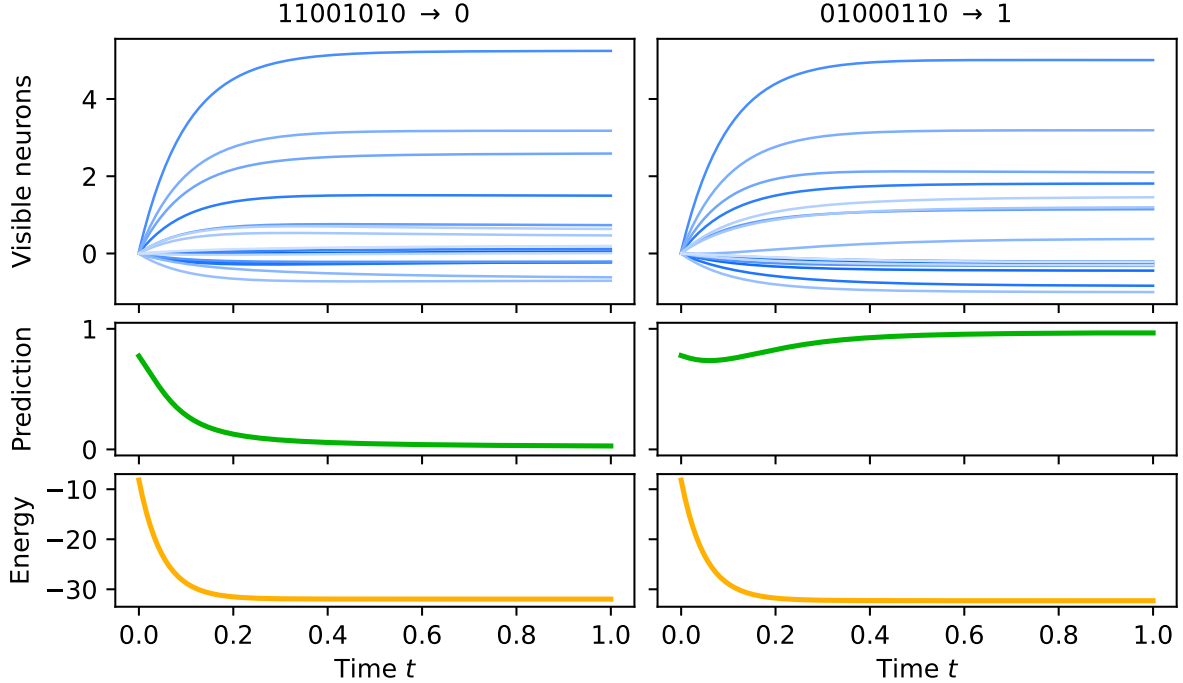


Figure 6: Inference of parity Analog ET on two example 8-bit strings. Top row plots the visible neurons v_i over time, middle row plots the decoded token prediction, bottom row plots the energy that monotonically decreases during inference. After a transient period of computation, the network arrives at a steady-state, making the result of the computation robust against the precise timing of the readout.

our experiments we simulate the dynamics of hardware with the Diffraex [32] ODE solver library. On the 8-bit parity task, our model achieves 100% accuracy on the hold-out validation set of 52 bit strings, demonstrating clear generalization capabilities. See Appendix H.1 for more details on training and model design.

Figure 6 shows the dynamics of the visible neurons and energy during two example inference runs of the Analog ET. Notably, the visible neuron values are constant by the end of the inference period, meaning that the inference remains highly stable to mismatch and delay in timing during readout. A single sample-and-hold and switching circuit would enable a single Analog-Digital Converter (ADC) to read out all the visible neurons at convergence, significantly reducing mismatch, and drastically saving device area, complexity, and energy. The intrinsic stability of attractor points arises uniquely from the continuous-time dynamics of the DenseAM, making these models particularly well suited to analog hardware.

6.2 Autoregressive inference

Dashed lines in Figure 5 illustrate the autoregressive inference procedure of the Analog ET. To generate the L -th token given context tokens $\mathbf{x}^{(1)}, \dots, \mathbf{x}^{(L-1)}$, each token is first embedded and concatenated to form the attention weight matrix

$$\boldsymbol{\xi}^{\text{attn},(L-1)} = \begin{bmatrix} \mathbf{e}^{(1)} \\ \mathbf{e}^{(2)} \\ \vdots \\ \mathbf{e}^{(L-1)} \end{bmatrix} \in \mathbb{R}^{(L-1) \times D}$$

These rows are loaded into the Analog ET’s energy attention weight matrix $\boldsymbol{\xi}^{\text{attn}}$ by programming the corresponding crossbar resistances. During inference, the visible state $\mathbf{v}(t)$ evolves according to the Analog ET dynamics until convergence. A decoder readout (e.g., a linear layer) applied to the converged $\mathbf{v}(t = T)$ values produces logits, from which the next token $\mathbf{x}^{(L)}$ is sampled. This token is then embedded to form $\mathbf{e}^{(L)}$, and appended to the existing context. The cycle repeats with the updated attention weight

matrix

$$\boldsymbol{\xi}^{\text{attn},(L)} = \begin{bmatrix} \boldsymbol{\xi}^{\text{attn},(L-1)} \\ \mathbf{e}^{(L)} \end{bmatrix} \in \mathbb{R}^{L \times D}$$

which now includes the new embedding $\mathbf{e}^{(L)}$. In hardware, this corresponds to connecting an additional hidden neuron in the energy attention block of Figure 5, and setting its resistive weights with $\mathbf{e}^{(L)}$. Because the physical order of hidden neurons does not affect the energy function, this new neuron can be placed in any position among the hidden neurons. When the context length is fixed, the hidden neuron corresponding to the earliest token can simply be reprogrammed with the new vector of weights $\mathbf{e}^{(L)}$, resulting in the hardware equivalent of a sliding-window context. In practice, an external digital controller, e.g., an Field-Programmable Gate Array (FPGA) or Application-Specific Integrated Circuit (ASIC) would orchestrate crossbar programming and token decoding, while the DenseAM dynamics perform the far more substantial workload of computing each next-token embedding.

This procedure is analogous to key-value (KV) caching in standard transformer inference [33]. Context tokens $\mathbf{x}^{(1)}, \dots, \mathbf{x}^{(L-1)}$ produce key and value vectors $\mathbf{k}^{(1)}, \dots, \mathbf{k}^{(L-1)}$ and $\mathbf{v}^{(1)}, \dots, \mathbf{v}^{(L-1)}$ respectively. When new token $\mathbf{x}^{(L)}$ is generated, its corresponding $\mathbf{k}^{(L)}$ and $\mathbf{v}^{(L)}$ vectors are appended to the cache, allowing all previous $\mathbf{k}^{(<L)}$ and $\mathbf{v}^{(<L)}$ to be reused without recomputation. When the key and value matrices are tied so that $\mathbf{k}^{(A)} = \mathbf{v}^{(A)}$, the ET’s row-append operation is equivalent to the standard KV-cache update. The ET performs an autoregressive rollout that reproduces the same recurrence structure as KV-cached transformer inference, but implemented physically through the addition of new neurons and weights without touching existing hardware. For a formal derivation of the equivalence between ET attention and conventional attention with tied keys and values, see [12].

7 Scaling properties

Inference time and energy consumption are crucial characteristics of our system. This section investigates these metrics with respect to the network size.

7.1 Inference time scaling

The model (4) and (5) is considered. In the adiabatic limit ($\tau_h \rightarrow 0$), which is satisfied by our hardware implementation, the time derivative of the energy can be written as

$$\frac{dE^{\text{eff}}}{dt} = \sum_{i=1}^{N_v} \frac{\partial E^{\text{eff}}}{\partial v_i} \frac{dv_i}{dt} = -\frac{1}{\tau_v} \sum_{i=1}^{N_v} \left(\frac{\partial E^{\text{eff}}}{\partial v_i} \right)^2 \sim -\frac{N_v}{\tau_v} \quad (12)$$

This derivative is always negative, since the dynamical system performs the gradient descent on the energy landscape. The derivative vanishes eventually when the network state vector \mathbf{v} converges to the steady state. Since the state vector v_i is typically initialized in the vicinity of the memory vectors, which are chosen to be of order one (~ 1), the right hand side of (4) is of order one too, independent of the network size. This results in the characteristic value of the temporal derivative shown in (12).

At the same time, the typical value¹ of the energy (5) is

$$|E^{\text{eff}}| \sim N_v + \frac{1}{\beta} \log(N_h) \quad (13)$$

During the inference dynamics the network is initialized in a high energy state, which has the characteristic value of energy (13), and performs energy descent to a lower value of the energy (which has a similar order of magnitude). In order to estimate the scaling of the time required to perform this energy descent, one can take a ratio of the energy drop by the rate of the energy decrease (12). This gives the following estimate

$$T^{\text{conv}} \sim \frac{|E^{\text{eff}}|}{\left| \frac{dE}{dt} \right|} \sim \tau_v \left(1 + \frac{1}{\beta} \frac{\log(N_h)}{N_v} \right) \sim \tau_v \quad (14)$$

The last \sim sign holds since in none of the designs presented here does N_h grow super-exponentially in N_v . In fact, in all the use cases N_h is sub-exponential in N_v .

¹We estimate the absolute value of the energy, since it can be both positive and negative depending on the mutual arrangement of memories, the state vector, and the number of hidden units.

This back-of-the-envelope estimation provides the core intuition behind the scaling relationship. The inference time is **constant**, and independent of the size of the network. A more careful analysis (Appendix E) shows that in the high- β regime the worst-case dependence is $\mathcal{O}\left(\frac{\tau_v}{\beta} \frac{\log N_h}{N_v}\right)$, which remains bounded for all architectures we consider. Thus, for our settings the convergence time is effectively constant in N_v and N_h . Based on amplifier gain-bandwidth, slew-rate, and output-current constraints, we estimate achievable inference times of tens to hundreds of nanoseconds using existing CMOS technology (see Appendix I.2).

7.2 Scaling of energy consumption

We now analyze how the total inference energy scales with network size. Energy dissipation arises primarily from (i) Ohmic loss in the resistive weights, (ii) charging of neuron-state capacitors, and (iii) constant per-neuron overhead from amplifiers and bias currents. We show that, under bounded voltage swings and fixed conductance budgets, total energy grows only linearly with the number of neurons.

Weight dissipation. Let the neuron output voltages be proportional to activations: $\mathbf{u} = \kappa \mathbf{g}$ and $\mathbf{w} = \kappa \mathbf{f}$, where κ is a fixed voltage swing. Such a bounded swing can always be enforced by global rescaling of ξ , β , and voltage units without changing the dynamics (see Appendix F). The instantaneous power dissipated by the resistive crossbar array is

$$P_{\text{weights}}(t) = \sum_{\mu=1}^{N_h} \sum_{i=1}^{N_v} \xi_{\mu i} (u_i - w_{\mu})^2 \quad (15)$$

With $0 \leq g_i \leq 1$, \mathbf{f} -softmax, and row/column conductance budgets $\sum_{\mu} \xi_{\mu i} \leq C_c$, $\sum_i \xi_{\mu i} \leq C_r$, the total power obeys

$$P_{\text{weights}}(t) \leq 2\kappa^2 (C_c N_v + C_r) = \mathcal{O}(N_v) \quad (16)$$

For a runtime of duration $T \sim T^{\text{conv}}$, the energy dissipated by the weights is therefore $E_{\text{weights}} = \mathcal{O}(N_v T)$, where $T \sim 1$ from subsection 7.1.

Capacitive and overhead energy. Each neuron charges a local capacitor a finite number of times by at most $V_{\text{swing}} \sim \kappa$, giving

$$E_{\text{cap}} \leq \kappa^2 \left(\sum_i C_i^{(v)} + \sum_{\mu} C_{\mu}^{(h)} \right) = \mathcal{O}(N_v + N_h) \quad (17)$$

Active bias and amplifier inefficiencies contribute fixed per-neuron power, yielding $E_{\text{other}} = \mathcal{O}((N_v + N_h)T)$.

Total energy scaling. With bounded voltage swing and conductance budgets,

$$E_{\text{total}} = \mathcal{O}(N_v + N_h) \quad (18)$$

Hence, the total inference energy scales only linearly with system size. For the full derivation, see Appendix G.

7.3 Scaling of hardware area

The area is dominated by two components: the area taken up by the synaptic weights, which is implemented as a crossbar array with programmable weights, and the area taken up by the neurons feeding the crossbar array. The area of the crossbar array scales as the number of weights $\mathcal{O}(N_v N_h)$. The area of the neurons scales as $\mathcal{O}(N_v + N_h)$.

8 Conclusion

In this paper, we have presented an analog accelerator architecture for Dense Associative Memories, implemented using resistive crossbar arrays and continuous-time RC neuron dynamics. Our design implements DenseAM inference as time evolution of a physical dynamical system, rather than a sequence of

discrete numerical update steps. We demonstrated this architecture with three representative settings of increasing complexity: XOR, Hamming (7,4) error decoding, and an Energy Transformer-style sequence model. These examples show that the analog DenseAM accelerator architecture covers both associative memory tasks and attention-based sequence models.

Our analysis shows that DenseAM accelerators enjoy favorable asymptotic scaling properties. Inference time is constant in the dimensions of the model size, meaning that inference time is governed primarily by the physical time constants of the circuit. This is in sharp contrast to digital implementations of the same dynamics, whose runtime must grow at least linearly with model size.

To assess hardware feasibility, we derived lower bounds on the neuronal time constants imposed by amplifier gain-bandwidth product, slew rate, and output current limits in our neuron design. Reported figures from representative CMOS OTAs in the literature give inference times on the order of tens-to-hundreds of nanoseconds, even with conservative design margins. Combined with the constant scaling of inference with model size, these estimates suggest that DenseAM accelerators can match or exceed the latency of digital GPUs as models grow, without requiring exotic devices or beyond-CMOS technologies.

Our results highlight DenseAMs as a natural abstraction for analog AI hardware. Their error correcting dynamics and asymptotic stability directly address long-standing concerns about robustness and readout timing: small perturbations are corrected by the dynamics instead of accumulated, and the final state is stable when readout happens over a wide temporal window. At the same time, the DenseAM framework is expressive enough to capture modern primitives such as attention and transformer-like architectures, as illustrated by our Analog Energy Transformer construction. These properties suggest that DenseAM-based analog accelerators may be a promising substrate for future AI systems, and motivate further co-design of models, dynamics, and devices.

Acknowledgements

MGB would like to thank Faiz Muhammad for exploratory attempts at SPICE simulations. DK would like to thank Kwabena Boahen for helpful discussions.

References

- [1] Ashish Vaswani. “Attention is all you need”. In: *arXiv preprint arXiv:1706.03762* (2017).
- [2] Jascha Sohl-Dickstein et al. “Deep unsupervised learning using nonequilibrium thermodynamics”. In: *International conference on machine learning*. pmlr. 2015, pp. 2256–2265.
- [3] Norman P Jouppi et al. “In-datacenter performance analysis of a tensor processing unit”. In: *Proceedings of the 44th annual international symposium on computer architecture*. 2017, pp. 1–12.
- [4] Eric Masanet et al. “Recalibrating global data center energy-use estimates”. In: *Science* 367.6481 (2020), pp. 984–986.
- [5] David Patterson et al. “Carbon emissions and large neural network training”. In: *arXiv preprint arXiv:2104.10350* (2021).
- [6] Maxwell Aifer et al. “Solving the compute crisis with physics-based ASICs”. In: *arXiv preprint arXiv:2507.10463* (2025).
- [7] Dmitry Krotov and John J Hopfield. “Dense associative memory for pattern recognition”. In: *Advances in neural information processing systems* 29 (2016).
- [8] Dmitry Krotov and John Hopfield. “Dense associative memory is robust to adversarial inputs”. In: *Neural computation* 30.12 (2018), pp. 3151–3167.
- [9] John J Hopfield. “Neural networks and physical systems with emergent collective computational abilities.” In: *Proceedings of the national academy of sciences* 79.8 (1982), pp. 2554–2558.
- [10] Dmitry Krotov and John J Hopfield. “Large Associative Memory Problem in Neurobiology and Machine Learning”. In: *International Conference on Learning Representations*. 2021.
- [11] Hubert Ramsauer et al. “Hopfield networks is all you need”. In: *arXiv preprint arXiv:2008.02217* (2020).
- [12] Benjamin Hoover et al. “Energy transformer”. In: *Advances in Neural Information Processing Systems* 36 (2024).

- [13] Benjamin Hoover et al. “Memory in plain sight: A survey of the uncanny resemblances between diffusion models and associative memories”. In: *arXiv preprint arXiv:2309.16750* (2023).
- [14] Luca Ambrogioni. “In search of dispersed memories: Generative diffusion models are associative memory networks”. In: *arXiv preprint arXiv:2309.17290* (2023).
- [15] Bao Pham et al. “Memorization to generalization: Emergence of diffusion models from associative memory”. In: *arXiv preprint arXiv:2505.21777* (2025).
- [16] Dmitry Krotov et al. “Modern methods in associative memory”. In: *arXiv preprint arXiv:2507.06211* (2025).
- [17] JJ Hopfield. “The effectiveness of analogue’neural network’hardware”. In: *Network: Computation in Neural Systems* 1.1 (1990), p. 27.
- [18] Dmitry Krotov. “Hierarchical associative memory”. In: *arXiv preprint arXiv:2107.06446* (2021).
- [19] Fei Tang and Michael Kopp. “A remark on a paper of krotov and hopfield [arxiv: 2008.06996]”. In: *arXiv preprint arXiv:2105.15034* (2021).
- [20] Benjamin Hoover et al. “A universal abstraction for hierarchical hopfield networks”. In: *The Symbiosis of Deep Learning and Differential Equations II*. 2022.
- [21] John J Hopfield. “Neurons with graded response have collective computational properties like those of two-state neurons.” In: *Proceedings of the national academy of sciences* 81.10 (1984), pp. 3088–3092.
- [22] David W Tank and John J Hopfield. “Simple “Neural” optimization networks: an A/D converter, signal decision circuit, and a linear programming circuit”. In: *Artificial neural networks: theoretical concepts*. 1988, pp. 87–95.
- [23] HP Graf et al. “VLSI implementation of a neural network memory with several hundreds of neurons”. In: *AIP conference proceedings*. Vol. 151. 1. American Institute of Physics. 1986, pp. 182–187.
- [24] Xinjie Guo et al. “Modeling and experimental demonstration of a Hopfield network analog-to-digital converter with hybrid CMOS/memristor circuits”. In: *Frontiers in neuroscience* 9 (2015), p. 488.
- [25] SG Hu et al. “Associative memory realized by a reconfigurable memristive Hopfield neural network”. In: *Nature communications* 6.1 (2015), p. 7522.
- [26] Sukru B Eryilmaz et al. “Brain-like associative learning using a nanoscale non-volatile phase change synaptic device array”. In: *Frontiers in neuroscience* 8 (2014), p. 205.
- [27] Brendan P Marsh et al. “Enhancing associative memory recall and storage capacity using confocal cavity QED”. In: *Physical Review X* 11.2 (2021), p. 021048.
- [28] Khalid Musa et al. “Dense Associative Memory in a Nonlinear Optical Hopfield Neural Network”. In: *arXiv preprint arXiv:2506.07849* (2025).
- [29] Carver Mead and Mohammed Ismail. *Analog VLSI implementation of neural systems*. Vol. 80. Springer Science & Business Media, 2012.
- [30] Richard W Hamming. “Error detecting and error correcting codes”. In: *The Bell system technical journal* 29.2 (1950), pp. 147–160.
- [31] Paul J Werbos. “Backpropagation through time: what it does and how to do it”. In: *Proceedings of the IEEE* 78.10 (2002), pp. 1550–1560.
- [32] Patrick Kidger. “On Neural Differential Equations”. PhD thesis. University of Oxford, 2021.
- [33] Zihang Dai et al. “Transformer-xl: Attentive language models beyond a fixed-length context”. In: *Proceedings of the 57th annual meeting of the association for computational linguistics*. 2019, pp. 2978–2988.
- [34] Jacob Sillman. “Analog Implementation of the Softmax Function”. In: *arXiv preprint arXiv:2305.13649* (2023).
- [35] John J Hopfield and David W Tank. “Computing with neural circuits: A model”. In: *Science* 233.4764 (1986), pp. 625–633.
- [36] Aldo Pena Perez and Franco Maloberti. “Performance enhanced op-amp for 65nm CMOS technologies and below”. In: *2012 IEEE International Symposium on Circuits and Systems (ISCAS)*. IEEE. 2012, pp. 201–204.

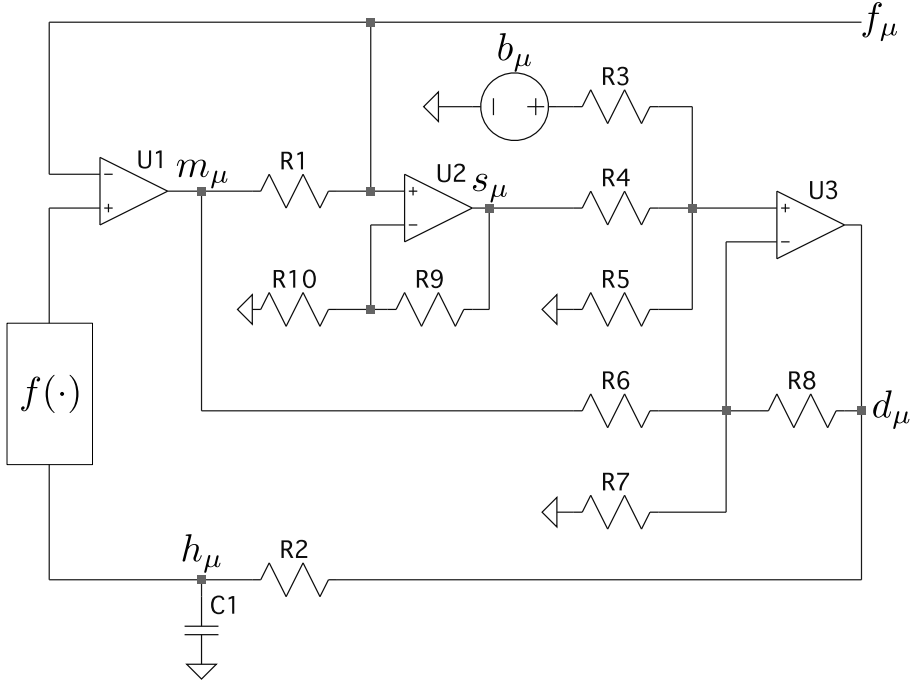


Figure 7: Circuit for a single neuron.

- [37] Rida S Assaad and Jose Silva-Martinez. “The recycling folded cascode: A general enhancement of the folded cascode amplifier”. In: *IEEE Journal of Solid-State Circuits* 44.9 (2009), pp. 2535–2542.
- [38] Alec Yen and Benjamin J Blalock. “A High Slew Rate, Low Power, Compact Operational Amplifier Based on the Super-Class AB Recycling Folded Cascode”. In: *2020 IEEE 63rd International Midwest Symposium on Circuits and Systems (MWSCAS)*. IEEE. 2020, pp. 9–12.
- [39] Mohammad H Naderi, Suraj Prakash, and Jose Silva-Martinez. “Operational transconductance amplifier with class-B slew-rate boosting for fast high-performance switched-capacitor circuits”. In: *IEEE Transactions on Circuits and Systems I: Regular Papers* 65.11 (2018), pp. 3769–3779.
- [40] Franz Schlögl and Horst Zimmermann. “A design example of a 65 nm CMOS operational amplifier”. In: *International Journal of Circuit Theory and Applications* 35.3 (2007), pp. 343–354.

A Neuron Design

Figure 7 shows the circuit design of a single neuron, with labels corresponding to this being a hidden neuron at index μ . We derive the dynamics of the neuron internal state h_μ and activation output voltage f_μ . We proceed using only Kirchhoff's Current Law (KCL) and the definition of an ideal op-amp.

Assumptions and conventions.

- **Ideal op-amps:** infinite open-loop gain, infinite input impedance (no input current), zero output impedance. Under stable negative feedback this enforces a virtual short $V_+ = V_-$.
- **Current J_μ :** we define J_μ as the current which flows from f_μ to m_μ through R_1 .
- **Op-amp input labels:** We denote the inverting and noninverting inputs of each op-amp explicitly, e.g. $U2_-$ for the inverting input of $U2$, $U3_+$ for the noninverting input of $U3$, etc.
- **Node labels:** Label m_μ as the output of $U1$, s_μ as the output of $U2$, and d_μ as the output of $U3$. The neuron pre-activation state is labeled h_μ , and the post-activation state is labeled f_μ . Voltage b_μ (as an ideal voltage source) drives the bias for this neuron. Voltages h_μ , b_μ , and f_μ correspond directly to the state variables in equation (1).

Block U1: buffer of activation voltage f_μ . Op-amp U1 buffers the output of the activation function $f(\cdot)$ and drives the output of the neuron, f_μ . Because no current can flow into $U1_-$, all the current flowing into this neuron must flow through R_1 to m_μ and is sourced or sunk by U1's output node.

Block U2: non-inverting stage producing s_μ from f_μ and m_μ . The positive input of U2 is $U2_+ = f_\mu$, and by U2's virtual short, the negative input $U2_- = U2_+ = f_\mu$. By KCL at $U2_-$,

$$\frac{U2_-}{R_{10}} = \frac{s_\mu - U2_-}{R_9} \Rightarrow s_\mu = \left(1 + \frac{R_9}{R_{10}}\right) f_\mu \quad (19)$$

Block U3: non-inverting stage producing d_μ from s_μ , b_μ , and m_μ . By KCL at the positive input of U3,

$$\frac{b_\mu - U3_+}{R_3} + \frac{s_\mu - U3_+}{R_4} = \frac{U3_+}{R_5} \Rightarrow U3_+ = \frac{R_4 R_5 b_\mu + R_3 R_5 s_\mu}{R_4 R_5 + R_3 R_5 + R_3 R_4} \quad (20)$$

KCL at the negative input of U3 gives us

$$\frac{m_\mu - U3_-}{R_6} + \frac{-U3_-}{R_7} = \frac{U3_- - d_\mu}{R_8} \Rightarrow d_\mu = U3_- \left(1 + R_8 \left(\frac{1}{R_6} + \frac{1}{R_7}\right)\right) - \frac{R_8 m_\mu}{R_6} \quad (21)$$

Virtual short of U3 means $U3_- = U3_+$. Combining equations (20) and (21), get

$$d_\mu = \frac{R_6 R_7 + R_8 (R_6 + R_7)}{R_6 R_7} \cdot \frac{R_4 R_5 b_\mu + R_3 R_5 s_\mu}{R_4 R_5 + R_3 R_5 + R_3 R_4} - \frac{R_8 m_\mu}{R_6} \quad (22)$$

Dynamics of RC circuit. R_2 and C_1 form an RC circuit driven by voltage d_μ . The voltage across the capacitor h_μ follows the relation

$$\begin{aligned} R_2 C_1 \frac{dh_\mu}{dt} &= -h_\mu + d_\mu \\ &= -h_\mu + \frac{R_6 R_7 + R_8 (R_6 + R_7)}{R_6 R_7} \cdot \frac{R_4 R_5 b_\mu + R_3 R_5 s_\mu}{R_4 R_5 + R_3 R_5 + R_3 R_4} - \frac{R_8 m_\mu}{R_6} \end{aligned} \quad (23)$$

With incoming current. Take the incoming current $J_\mu = \sum_i \xi_{\mu i} (g_i - f_\mu)$. This produces a voltage drop across R_1 such that $m_\mu = f_\mu - R_1 J_\mu = f_\mu - R_1 \sum_i \xi_{\mu i} (g_i - f_\mu)$. Then, the dynamics of h_μ from equation (23) are

$$R_2 C_1 \frac{dh_\mu}{dt} = -h_\mu + \frac{R_6 R_7 + R_8 (R_6 + R_7)}{R_6 R_7} \cdot \frac{R_4 R_5 b_\mu + R_3 R_5 s_\mu}{R_4 R_5 + R_3 R_5 + R_3 R_4} - \frac{R_8}{R_6} (f_\mu - R_1 J_\mu) \quad (24)$$

Substituting in s_μ from equation (19) and J_μ :

$$R_2 C_1 \frac{dh_\mu}{dt} = -h_\mu + \frac{R_6 R_7 + R_8 (R_6 + R_7)}{R_6 R_7} \cdot \frac{R_4 R_5 b_\mu + R_3 R_5 \left(1 + \frac{R_9}{R_{10}}\right) f_\mu}{R_4 R_5 + R_3 R_5 + R_3 R_4} - \frac{R_8}{R_6} \left(f_\mu - R_1 \sum_i \xi_{\mu i} (g_i - f_\mu)\right) \quad (25)$$

Equal-resistance special case. Set $R_1 = R_3 = R_4 = R_5 = R_6 = R_7 = R_8$. Then, equation (25) reduces to

$$R_2 C_1 \frac{dh_\mu}{dt} = -h_\mu + b_\mu + \frac{R_9}{R_{10}} f_\mu + \sum_i \xi_{\mu i} (g_i - f_\mu) \quad (26)$$

Selection of R_9/R_{10} self-term gain. Evidently, in order to match the form of equation (1), we need to cancel the $-f_\mu \sum_i \xi_{\mu i}$ term that appears on the right hand side of equation (26). The R_9/R_{10} term allows us to do that by setting

$$\frac{R_9}{R_{10}} = \sum_i \xi_{\mu i} \quad (27)$$

Taking equation (27)'s assignment to R_9 and R_{10} simplifies equation (26) into

$$R_2 C_1 \frac{dh_\mu}{dt} = \sum_i \xi_{\mu i} g_i - h_\mu + b_\mu \quad (28)$$

which exactly matches our desired dynamics.

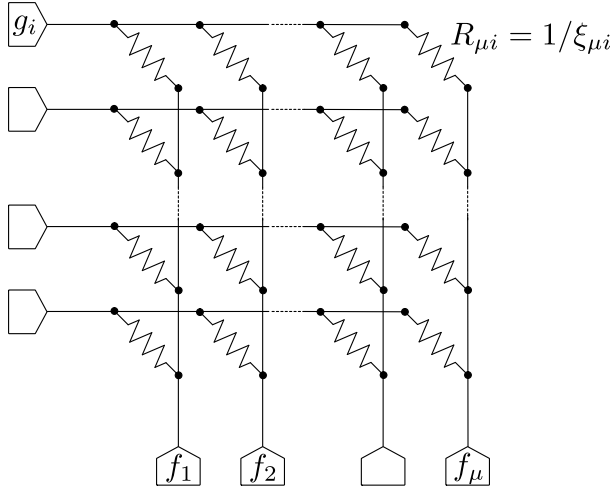


Figure 8: Crossbar Array. Each pentagon contains a neuron of design in Figure 7. In this layout we have flipped the crossbar array, so that index μ runs horizontally and index i runs vertically.

A.1 Activation function

The voltage across C_1 gives us the dynamics of the neuron internal state h_μ . Figure 7 contains a block representing a nonlinear amplifier, denoted $f(\cdot)$, whose input is h_μ and whose output is $f_\mu = f(h_\mu)$. This voltage is buffered with U1 onto the neuron output line, labeled f_μ , which is what other neurons “see” in the crossbar array. The chosen activation function does not affect the rest of the dynamics of the neuron. Particularly, the activation function need not be element-wise: a vector-wise activation function like softmax can be readily applied instead.

A.2 Neurons interacting in a network

So far we have examined the dynamics of a single neuron, treating as an assumption that the neuron will receive an incoming current $J_\mu = \sum_i \xi_{\mu i} (g_i - f_\mu)$. Now, we will show how to wire these neurons together to realize this. Figure 8 shows the simplest DenseAM construction where each pentagonal node is a circuit of design in Figure 7. Each neuron exposes a single node whose voltage is driven at the activation of the neuron, and which accepts an incoming current which it uses to drive its dynamics. Each hidden neuron f_μ is connected to a visible neuron g_i via a resistance $R_{\mu i} = 1/\xi_{\mu i}$ that is the inverse of the weight it represents. The current flowing into node f_μ is $J_\mu = \sum_i \frac{1}{R_{\mu i}} (g_i - f_\mu)$, which is the assumption needed for equation (24). This same analysis holds for other hidden and visible neurons, and so together they realize the large dynamical system of (1).

A.3 SPICE Netlist

Following is the SPICE netlist for the single neuron circuit, using ideal op-amps. Component values are omitted for brevity. There is no nonlinearity here; adding one would be a matter of inserting a nonlinear amplifier between node h_μ and XU1’s positive terminal.

```

R1 f_μ m_μ
XU1 f_μ h_μ m_μ opamp Aol=100K GBW=10Meg
XU2 u2- f_μ s_μ opamp Aol=100K GBW=10Meg
R2 u2- 0
R3 s_μ u2-
R4 u3+ s_μ
R5 u3+ 0
XU3 u3- u3+ d_μ opamp Aol=100K GBW=10Meg
R6 u3- m_μ
R7 d_μ u3-
R8 d_μ h_μ
C1 h_μ 0

```

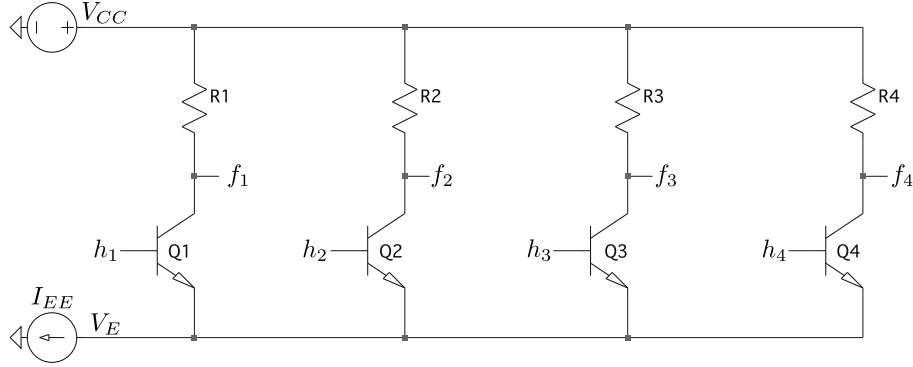


Figure 9: Softmax circuit design

```

V$B_p N001 0
R9 u3+ N001
R10 u3- 0

```

B Softmax Circuit

For demonstration purposes, we follow the construction of an analog softmax circuit using bipolar junction transistors (BJTs) described in [34]. Figure 9 shows the design of a four-way softmax circuit using BJTs. The softmax function we aim to produce is:

$$\text{softmax}_i = \frac{e^{z_i}}{\sum_{j=1}^N e^{z_j}}, \quad i = 1, \dots, N \quad (29)$$

For the μ th BJT in the circuit, the collector current $I_{C,\mu}$ can be expressed in terms of the base voltage h_μ and the emitter voltage V_E when in the forward-active mode as:

$$I_{C,\mu} = I_s e^{V_{BE}/V_T}, \quad V_{BE,\mu} = h_\mu - V_E, \quad \Rightarrow \quad I_{C,\mu} = I_s e^{\frac{h_\mu - V_E}{V_T}} \quad (30)$$

where I_s is the BJT's saturation current and V_T is the thermal voltage. Assuming large BJT β (note: this β is unrelated to the softmax β)², we can neglect base currents $I_{C,\mu} = I_{E,\mu}$. Applying KCL at the shared emitter node V_E , the total current $I_{EE} = \sum_{\mu=1}^N I_{C,\mu}$. We can expand the expression for the collector currents to get the currents in terms of node voltages:

$$\begin{aligned} I_{EE} &= \sum_{\mu=1}^{N_h} I_s e^{(h_\mu - V_E)/V_T} \\ &= \sum_{\mu=1}^{N_h} \frac{I_s e^{h_\mu/V_T}}{e^{V_E/V_T}} \end{aligned} \quad (31)$$

Simultaneously, the current I_{EE} is also fixed by the ideal current source, so $I_{C,\mu}$ can also be expressed as the ratio of the branch current to the total current: $I_{C,\mu} = \frac{I_{C,\mu}}{I_{EE}} I_{EE}$. Plugging in (30) for $I_{C,\mu}$ and (31) for I_{EE} in the denominator and canceling the term containing V_E ,

$$I_{C,\mu} = \frac{e^{h_\mu/V_T}}{\sum_{j=1}^{N_h} e^{h_j/V_T}} I_{EE} \quad (32)$$

This already looks very much like the ideal softmax function. The voltage at node f_i is created by current flowing through resistor R_i , producing a voltage drop relative to V_{CC} . Specifically, the voltage $f_\mu = V_{CC} - \frac{e^{h_\mu/V_T}}{\sum_{j=1}^{N_h} e^{h_j/V_T}} I_{EE} R_\mu$. When $I_{EE} R_\mu = 1$, this voltage f_μ is a negated and shifted softmax in the range of 1 volt. This scale and negation can be easily corrected with an op amp, which is also needed to isolate the node and prevent loading. Note that V_{CC} must be chosen to be positive supply in order for the BJTs to remain in the forward-active mode.

²In BJTs, β denotes the ratio of the collector current to the base current. High BJT β indicates the transistor is able to amplify a small base current into a much larger collector current, allowing the BJT to function as an amplifier or switch. A high β reflects that the BJT can efficiently transmit carriers from emitter to collector, without losing them to the base.

Parameter	Value
R_F	1000 Ω
R_T	1 Ω
R_1	1 Ω
R_2, R_3, \dots, R_8	10 000 Ω
R_S	40 Ω
C	10 μF
a_3	0 V
b_1	0 V
b_2	-1 V
b_3	-1 V
b_4	-1 V

Table 2: Component and parameter values.

C XOR DenseAM Circuit

Figure 10 is a full circuit diagram of the DenseAM that solves the XOR problem. Given input voltages at $V1, V2 \in \{0, 1\}$, the output voltage at g_3 is the result of the XOR operation between $V1$ and $V2$. In this model, the visible neuron is linear, and the hidden neurons share a softmax activation function implemented by a set of bipolar junction transistors. Table 2 lists the component values used in simulation.

Visible neurons. In the XOR task, only one visible neuron is left evolving, corresponding to the output column of the truth table. As such, the first two neurons are clamped to the input voltages, represented by $V1$ and $V2$. The third visible neuron, highlighted in blue, is a linear unit with no nonlinear activation: the internal state voltage v_3 directly drives the output, setting $g_3 = v_3$. This is the same circuit described in Appendix A, except where the activation block is not present.

Hidden neurons. The XOR task requires four hidden neurons, highlighted in green. These are identical circuit constructions with the exception of the voltage sources b_μ for the biases, which are set according to the values in Table 2. Unlike the visible neuron, the hidden neurons have a softmax activation function, such that $f_\mu = \text{softmax}_\mu(h)$.

Softmax activation function. The red highlights the same softmax circuit described in Appendix B, comprised of BJT transistors, resistors, a voltage source for V_{CC} and a current source for I_{EE} . We use the 2N5088 transistors in our model, reflecting a standard and widely available BJT. Noninverting buffers (U10, U11, etc.) are used to prevent loading effects on the state capacitors C_μ from current draw of the BJT base in forward-active mode. As discussed in Appendix B, the softmax circuit itself produces an output voltage of

$$\text{softmax}(z)_i = V_{CC} - \frac{e^{z_i}}{\sum_{j=1}^N e^{z_j}}, \quad i = 1, \dots, N$$

When $V_{CC} = 5V$ as in this circuit, this requires extra circuitry, highlighted in yellow, to shift and negate the softmax output. This is done by first buffering the voltage output to prevent loading effects, followed by a summing op amp that subtracts V_{CC} and inverts the softmax output. For the first hidden neuron h_1 (lower left of figure), op-amp U2 buffers the voltage output, while U1 is configured in an inverting summing configuration to add -5V (the inverse of V_{CC}) to the buffered voltage output, producing the correct softmax output.

Weight matrix. The weight matrix is comprised of resistors R_1-R_{12} that represent the weight matrix ξ . These are set directly according to the XOR truth table, where each row corresponds to one hidden neuron. A boolean value of 1 (R_T) is set to be a high conductance (1Ω), while a boolean value of 0 (R_F) is set to be a relatively small conductance ($1\text{k}\Omega$).

The gain s_i/g_i governing the value of s_i is set to be the sum of the resistances in that neuron's crossbar column. The column of resistances for neuron 1 has 3 R_F resistances, which sum to 3×10^{-3} . Hence,

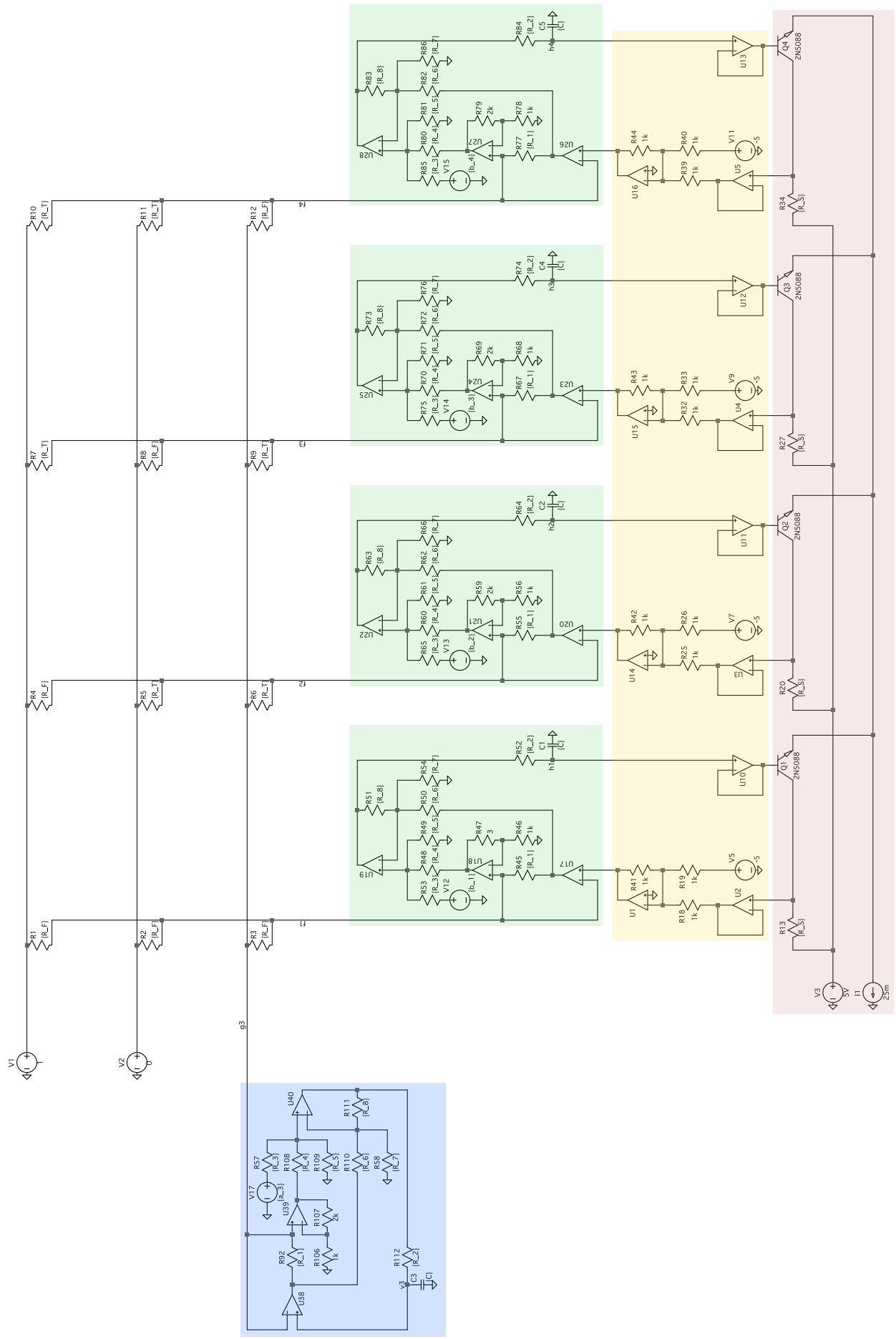


Figure 10: Full schematic for XOR DenseAM built with 1 evolving linear visible neuron and 4 hidden neurons with softmax activation. **Blue:** visible neuron. **Green:** hidden neurons. **Yellow:** buffers for softmax activation circuit. **Red:** analog softmax circuit.

neuron 1's $R_{47}/R_{R46} = 3/1000$. The crossbar resistances for neuron 2, 3, and 4 have 2 R_T resistances and one R_F resistance, which sums to approximately 2. Hence, we approximate $R_{59}/R_{56} = 2000/1000$ and similarly for hidden neurons 3 and 4.

D Design and implementation variations

A large design space remains open across analog electronics and other substrates for realizing DenseAMs, with clear speed–energy–area–precision trade-offs. In electronics, the core primitives admit multiple realizations: passive, nonvolatile weights (e.g., memristors, triode-region or floating-gate transistors, and other programmable conductors); active, gained weights via OTAs; and nonlinearities via diode clamps, reverse-biased diode/BJT exponentials, MOS quadratic regions, or translinear blocks. Architectures in the spirit of [35, 23] are compact but couple synaptic values to neuronal time constants, making dynamics drift when a single weight changes—problematic for learning and consistent timing—whereas our decoupled neuron preserves a fixed time constant under weight updates. Simpler neuron/network topologies likely exist and can be attractive in resource-constrained regimes, provided their deviations from the target ODEs are validated not to degrade performance. Beyond CMOS, photonics (e.g., overdamped, low-Q microring resonators) can naturally implement first-order ODEs and can offer extreme bandwidth with distinct calibration and noise constraints. Across these options, open problems include robust weight storage/programmability and drift control, mixed-signal learning rules compatible with device limits, scaling under current/GBW/SR constraints, tolerance to mismatch/noise, and algorithm–circuit co-design to exploit substrate-specific advantages.

E Scaling of inference time

There are two conditions under which inference times should be studied, dependent on the softmax temperature β . In the low- β regime, the DenseAM reaches equilibria with multiple hidden neurons “competing” in the softmax, while in the high- β regime, the DenseAM reaches equilibria with only one hidden neuron “winning out” in the softmax. Intuitively, the high- β regime corresponds to exact memory recall, while the low- β regime corresponds to interpolation. The XOR and Hamming (7,4) code are in the high- β regime, while the energy transformer lies in the low- β regime. In both regimes, we find that the DenseAM converges in time that is constant with respect to the number of neurons.

Assumptions.

(A1) There is a per-synapse device limit of $0 \leq \xi_{\mu i} \leq G_{\max}$ where G_{\max} is the maximum conductance set by the physics of the crossbar crosspoints. Because f is the output of a softmax so $f_\mu \leq 1 \forall \mu$, this means

$$\sum_{\mu} \xi_{\mu i} f_{\mu} \leq G_{\max} \quad (33)$$

so the RHS of the visible neuron dynamics is $\mathcal{O}(1)$.

There exist both column-sum and row-sum budgets that are enforced by the hardware, since each neuron's output stage can only source/sink a finite amount of current while maintaining GBW/SR margins. This dictates a per-column and per-row conductance budget to stay within this maximum current, resulting in

$$\sum_i^{N_v} \xi_{\mu i} \leq C_r \quad \forall \mu, \quad \sum_{\mu} \xi_{\mu i} \leq C_c \quad \forall i \quad (34)$$

Weights can only be positive since conductances can only be positive, so $\xi_{\mu i} \geq 0$.

As a corollary of (A1), note also that we can bound $\|\xi_{\mu}\|_2 \leq S \forall \mu$, and since $\|\xi_{\mu}\|_2 \leq \|\xi_{\mu}\|_1$, then $\|\xi_{\mu}\|_2 \leq C_c \forall \mu$.

(A2) Bounded biases. $|a_i| \leq A$, $|b_{\mu}| \leq B$ for all i, μ . In realistic regimes, this typically holds, for example the typical choice in boolean functions of $b_{\mu} = -\frac{\beta}{2} \|\xi_{\mu}\|^2$ (seen in Section 5.1).

Model. Take the system of equation (1) with a softmax activation on hidden neurons and an identity activation on visible neurons. For clarity we assume 0 biases on visible neurons, but they do not change the analysis.

$$\tau_v \dot{\mathbf{v}} = \boldsymbol{\xi}^\top \mathbf{f} + \mathbf{a} - \mathbf{v}, \quad \tau_h \dot{\mathbf{h}} = \boldsymbol{\xi} \mathbf{v} + \mathbf{b} - \mathbf{h}, \quad \mathbf{f} = \text{softmax}_\beta(\mathbf{h}) \quad (35)$$

Integrating out the hidden units,

$$\tau_v \dot{\mathbf{v}} = \boldsymbol{\xi}^\top f(\mathbf{v}) - \mathbf{v}, \quad (36)$$

$$f(\mathbf{v}) = \text{softmax}(\beta(\boldsymbol{\xi} \mathbf{v} + \mathbf{b})) \quad (37)$$

yields the effective energy function expressed in terms of visible neurons:

$$E(\mathbf{v}) = \frac{1}{2} \|\mathbf{v}\|^2 - \frac{1}{\beta} \log \sum_\mu \exp \left(\beta (\boldsymbol{\xi}_\mu^\top \mathbf{v} + \mathbf{b}) \right) \quad (38)$$

where $\nabla E(\mathbf{v}) = \mathbf{v} - \boldsymbol{\xi}^\top f(\mathbf{v})$. Because $\tau_v \dot{\mathbf{v}} = -\nabla E(\mathbf{v})$, we see that the dynamical trajectory causes the energy to monotonically decrease over time:

$$\frac{d}{dt} E(\mathbf{v}(t)) = \nabla E(\mathbf{v}(t))^\top \dot{\mathbf{v}} = -\frac{1}{\tau_v} \|\nabla E(\mathbf{v}(t))\|^2 \leq 0 \quad (39)$$

E.1 Low- β regime

The energy landscape in the low- β regime exhibits uniform strong convexity, so the gradient flow dynamics cause the energy gap to decay exponentially, reaching an ϵ -fraction of the original energy gap in constant time. To show $E(\mathbf{v})$ is α -strongly convex, we must show $\nabla^2 E(\mathbf{v}) \succeq \alpha I$ for some $\alpha > 0$. This means that all the eigenvalues of the Hessian are $\geq \alpha$. Equivalently, $\lambda_{\min}(\nabla^2 E) \geq \alpha$. Denote $G(\mathbf{f}) = \text{Diag}(\mathbf{f}) - \mathbf{f}\mathbf{f}^\top \succeq 0$, which is the Jacobian of the softmax function $f(\mathbf{v}) = \text{softmax}(\beta(\boldsymbol{\xi} \mathbf{v} + \mathbf{b}))$.

$$\nabla^2 E(\mathbf{v}) = I - \beta \boldsymbol{\xi}^\top G(\mathbf{f}) \boldsymbol{\xi} \quad (40)$$

$$\lambda_{\min}(\nabla^2 E(\mathbf{v})) = \lambda_{\min}(I - \beta \boldsymbol{\xi}^\top G(\mathbf{f}) \boldsymbol{\xi}) \quad (41)$$

$$= 1 - \beta \lambda_{\max}(\boldsymbol{\xi}^\top G(\mathbf{f}) \boldsymbol{\xi}) \quad (42)$$

$$\Rightarrow \nabla^2 E(\mathbf{v}) \succeq (1 - \beta \lambda_{\max}(\boldsymbol{\xi}^\top G(\mathbf{f}) \boldsymbol{\xi})) I \quad (43)$$

Because $G(\mathbf{f}) \preceq \text{Diag}(\mathbf{f}) \preceq I$ is PSD and therefore $\boldsymbol{\xi} G(\mathbf{f}) \boldsymbol{\xi}^\top$ is also PSD, and $G(\mathbf{f})$ is a probability-weighted covariance where $\sum_\mu f_\mu = 1$,

$$\lambda_{\max}(\boldsymbol{\xi}^\top G(\mathbf{f}) \boldsymbol{\xi}) \leq \text{tr}(\boldsymbol{\xi}^\top G(\mathbf{f}) \boldsymbol{\xi}) \leq \sum_\mu f_\mu \|\boldsymbol{\xi}_\mu\|^2 \leq \max_\mu \|\boldsymbol{\xi}_\mu\|^2 \quad (44)$$

Denote $S^2 = \max_\mu \|\boldsymbol{\xi}_\mu\|^2 \leq C_c$ as in **(A1)**. Therefore, the Hessian of E can be bounded as

$$\nabla^2 E(\mathbf{v}) \succeq (1 - \beta S^2) I = \alpha I \quad (45)$$

where $\alpha = 1 - \beta S^2$. Then $\alpha > 0$ when $\beta < 1/\max_\mu \|\boldsymbol{\xi}_\mu\|^2$. This is a sufficient (but not necessary) condition for the system to be in the low- β (uniformly convex) regime, where the softmax is diffuse enough that its covariance term does not contribute so much negative curvature as to overwhelm the positive curvature contributed by the identity term. In this regime, the uniform lower bound on the Hessian implies α -strong convexity, which gives the PL inequality

$$\frac{1}{2} \|\nabla E(\mathbf{v})\|^2 \geq \alpha(E(\mathbf{v}) - E^*) \quad (46)$$

Together with (39), this allows us to bound the time constant of gradient flow:

$$\frac{d}{dt} (E(\mathbf{v}(t)) - E^*) = -\frac{1}{\tau_v} \|\nabla E(\mathbf{v}(t))\|^2 \leq -\frac{2\alpha}{\tau_v} (E(\mathbf{v}(t)) - E^*) \quad (47)$$

If the curvature is bounded below by α , then the gradient magnitude grows at least linearly with distance to the minimum, ensuring the energy function is “steep enough” to ensure exponential convergence. Integrating,

$$E(\mathbf{v}(t)) - E^* \leq (E(\mathbf{v}(0)) - E^*)e^{-\frac{2\alpha}{\tau_v}t} \quad (48)$$

This indicates exponential decay of the energy gap. In order to reach an ϵ -fraction of the original energy gap, this takes time

$$T(\epsilon) \leq \frac{\tau_v}{2\alpha} \log \frac{1}{\epsilon} = \mathcal{O}(\tau_v \log(1/\epsilon)) \quad (49)$$

which is entirely independent of system size N_v and N_h . In the energy transformer case, this means that convergence time is entirely independent of context length L and token dimension D .

E.2 High- β regime

E.2.1 T_I : Basin selection

Denote

$$s_\mu(\mathbf{v}) := \xi_\mu^\top \mathbf{v} + \mathbf{b}_\mu, \quad m(\mathbf{v}) := \max_\mu s_\mu(\mathbf{v}), \quad \mathbf{f} := \text{softmax}(\beta \mathbf{s}) \quad (50)$$

Define the basin of attraction around the winning softmax logit k by the margin $\gamma > 0$:

$$\mathcal{B}_k(\gamma) = \{\mathbf{v} : s_k(\mathbf{v}) - \max_{j \neq k} s_j(\mathbf{v}) \geq \gamma\} \quad (51)$$

Let T_I be the first time t such that $\mathbf{v}(t) \in \cup_k \mathcal{B}_k(\gamma)$. Defining the softmax component of the energy function (38) as

$$\text{LSE}_\beta(\mathbf{s}) = \frac{1}{\beta} \log \sum_{\mu=1}^{N_h} e^{\beta s_\mu}$$

then for every \mathbf{v} , we can bound the LSE as

$$m(\mathbf{v}) \leq \text{LSE}_\beta(s(\mathbf{v})) \leq m(\mathbf{v}) + \frac{1}{\beta} \log N_h \quad (52)$$

Thus, the “softmax slack” $\delta(\mathbf{v}) := \text{LSE}_\beta(s(\mathbf{v})) - m(\mathbf{v})$ obeys $0 \leq \delta(\mathbf{v}) \leq \frac{1}{\beta} \log N_h$. In the high- β regime, there are no critical points other than the softmax basins (those within $\cup_k \mathcal{B}_k(\gamma)$ for any reasonable $\gamma > \epsilon > 0$). To reduce δ from its initial value to the cusp of one of the basins requires dissipating at most

$$\Delta E_{\text{softmax}} \leq \frac{1}{\beta} \log N_h \quad (53)$$

$\frac{\partial E}{\partial v_i} = -\tau_v \dot{v}_i$, and outside winning basins $\tau_v \dot{v}_i \sim 1$, so the squared magnitude of the gradient grows at least linearly in N_v :

$$\|\nabla E(\mathbf{v})\|^2 = \sum_{i=1}^{N_v} \left(\frac{\partial E}{\partial v_i} \right)^2 \geq c N_v \quad (54)$$

for some $c > 0$ independent of N_v and N_h for all \mathbf{v} in the trajectory outside a winning basin. Therefore, the energy dissipation rate satisfies

$$-\dot{E}(t) = \frac{1}{\tau_v} \|\nabla E(\mathbf{v}(t))\|^2 \geq \frac{c}{\tau_v} N_v \quad (55)$$

Under assumptions **(A1)**–**(A2)**, the visible state \mathbf{v} remains in a bounded box, so the quadratic part of the energy contributes at most $\mathcal{O}(N_v)$ to the energy difference between any two points on the trajectory. Since the energy dissipation rate during T_I scales proportionally to N_v , the quadratic component of the energy contribution is dissipated in constant time. The only nontrivial N_h dependence is due to the softmax slack. Together with the bound on $\Delta E_{\text{softmax}}$, the total time this phase takes is characteristically

$$T_I = \mathcal{O} \left(\frac{\tau_v \log N_h}{\beta} \right) \quad (56)$$

E.2.2 T_{II} : Contractive convergence within a winning basin

Find a basin $\mathcal{B}_k(\gamma)$ that is entered at $t_{\text{in}} = T_I$. We will now show local strong convexity within this basin, allowing us to invoke the PL inequality and find exponential convergence within the basin. Define $G := \text{Diag}(\mathbf{f}) - \mathbf{f}\mathbf{f}^\top$. First, consider that the non-winning softmax mass is $1 - f_k$, which is

$$1 - f_k = \sum_{j \neq k} f_j \leq (N_h - 1)e^{-\beta\gamma} \quad (57)$$

Additionally, since $\|\mathbf{f}\|^2 = f_k^2 + \sum_{j \neq k} f_j^2 \geq f_k^2$ and $0 \leq f_k \leq 1$,

$$\lambda_{\max}(G(\mathbf{f})) \leq \text{tr}(G(\mathbf{f})) = 1 - \|\mathbf{f}\|^2 \leq 1 - f_k^2 \leq 2(1 - f_k) \leq 2(N_h - 1)e^{-\beta\gamma} \quad (58)$$

Hence, with $S^2 = \max_\mu \|\xi_\mu\|^2$,

$$\lambda_{\max}(\xi^\top G(\mathbf{f}) \xi) \leq S^2 \lambda_{\max}(G(\mathbf{f})) \leq 2S^2(N_h - 1)e^{-\beta\gamma} \quad (59)$$

This gives a bound on the largest eigenvalue of $G(\mathbf{f})$ in a way that incorporates the softmax beta.

Now, we can show local strong convexity in the winning basin:

$$\nabla^2 E(\mathbf{v}) = I - \beta \xi^\top G(\mathbf{f}) \xi \succeq (1 - \beta 2S^2(N_h - 1)e^{-\beta\gamma})I \equiv \alpha(\beta, \gamma)I \quad (60)$$

for all $\mathbf{v} \in \mathcal{B}_k(\gamma)$. Particularly, if

$$e^{-\beta\gamma}(N_h - 1) \leq \frac{1}{4\beta S^2} \quad (61)$$

then $\alpha(\beta, \gamma) \geq \frac{1}{2}$, independent of N_h, N_v . Note that this is always possible: if the softmax is not peaked enough to make this inequality true, simply keep moving in trajectory ‘‘Phase I’’ for a little longer until the margin γ grows slightly larger such that the condition holds true. This strong convexity within $\mathcal{B}_k(\gamma)$ implies the PL inequality

$$\frac{1}{2} \|\nabla E(\mathbf{v})\|^2 \geq \alpha(\beta, \gamma)(E(\mathbf{v}) - E^*), \quad \forall \mathbf{v} \in \mathcal{B}_k(\gamma) \quad (62)$$

Therefore, along the trajectory within the basin for times $t \geq t_{\text{in}}$,

$$\frac{d}{dt} (E(\mathbf{v}(t)) - E^*) = -\frac{1}{\tau_v} \|\nabla E(\mathbf{v}(t))\|^2 \leq -\frac{2\alpha(\beta, \gamma)}{\tau_v} (E(\mathbf{v}(t)) - E^*) \quad (63)$$

Integrating,

$$E(\mathbf{v}(t)) - E^* \leq e^{-\frac{2\alpha(\beta, \gamma)}{\tau_v}(t - t_{\text{in}})} (E(\mathbf{v}(t_{\text{in}})) - E^*) \quad (64)$$

Impose a relative-to-initial convergence criteria:

$$E(\mathbf{v}(t)) - E^* \leq \epsilon (E(\mathbf{v}(0)) - E^*), \quad \epsilon \in (0, 1)$$

Since E is non-increasing along the trajectory, $E(\mathbf{v}(t_{\text{in}})) - E^* \leq E(\mathbf{v}(0)) - E^*$, so it suffices that

$$e^{-\frac{2\alpha(\beta, \gamma)}{\tau_v}(t - t_{\text{in}})} \leq \epsilon$$

Hence the in-basin time satisfies

$$T_{II} \leq \frac{\tau_v}{2\alpha(\beta, \gamma)} \log \frac{1}{\epsilon} = \mathcal{O}\left(\tau_v \log \frac{1}{\epsilon}\right) \quad (65)$$

which is size-free of N_h and N_v .

E.2.3 Combined bound

Altogether, in the high- β regime, to reach a relative-to-initial tolerance of

$$E(\mathbf{v}(t)) - E^* \leq \epsilon (E(\mathbf{v}(0)) - E^*) \quad (66)$$

the combined convergence time satisfies

$$T(\epsilon) = \underbrace{\mathcal{O}\left(\frac{\tau_v \log N_h}{\beta N_v}\right)}_{\text{winner selection } (T_I)} + \underbrace{\mathcal{O}\left(\tau_v \log \frac{1}{\epsilon}\right)}_{\text{convergence within basin } (T_{II})} \quad (67)$$

For fixed ϵ , β , and τ_v , T_{II} is independent of N_v and N_h , while T_I carries all the model-size dependence. The dependence of the convergence time on N_h and N_v in the high- β regime is

$$T(\epsilon) = \mathcal{O}\left(\frac{\tau_v \log N_h}{\beta N_v}\right). \quad (68)$$

The convergence time is at most logarithmic in the number of hidden neurons N_h , and actually decreases as $1/N_v$ in the number of visible neurons.

E.3 Limitations

Our analysis assumes that the timescales of the crossbar array are much faster than the fastest neuronal timescales. In practice, as the crossbar array gets bigger, it may contribute to the time scales of the entire system, since wires have non-zero capacitances. Once the size of the crossbar array reaches the point when it significantly modifies the time scales of the neurons, our analysis and the scaling argument becomes invalid. For this reason, one cannot scale this design to infinitely large sizes. Analyzing that boundary is outside the scope of our paper, because it is dependent on fabrication and design parameters, which is a different level of abstraction than our present paper.

F Design invariance under voltage scaling

Given hardware constraints of G_{\max} , C_c , and C_r , we can still implement models with arbitrarily large weights. Convergence bounds rely on the weight matrix constraints, which can be made feasible by global normalization at the hardware level, keeping the effective model weights unchanged. Consider the scaling factor for any non-negative ξ :

$$\kappa = \min \left\{ 1, \frac{G_{\max}}{\max_{\mu,i} \xi_{\mu i}}, \frac{C_c}{\max_i \sum_{\mu} \xi_{\mu i}}, \frac{C_r}{\max_{\mu} \sum_i \xi_{\mu i}} \right\} \quad (69)$$

Set $\tilde{\xi} = \kappa \xi$. Then, $\tilde{\xi}$ satisfies all the hardware constraints of assumption **(A1)**:

$$0 \leq \tilde{\xi}_{\mu i} \leq G_{\max}, \quad \sum_i \tilde{\xi}_{\mu i} \leq C_r \quad \forall \mu, \quad \sum_{\mu} \tilde{\xi}_{\mu i} \leq C_c \quad \forall i \quad (70)$$

So any ξ matrix can be mapped onto budgets with one scalar κ . Consider the pre-softmax arguments for the hidden neurons: if we scale weights $\xi \rightarrow \tilde{\xi} = \kappa \xi$, rescale the voltage unit $\mathbf{v} \rightarrow \tilde{\mathbf{v}} = \kappa \mathbf{v}$ and biases $\mathbf{b} \rightarrow \tilde{\mathbf{b}} = \kappa^2 \mathbf{b}$ and set $\tilde{\beta} = \beta/\kappa^2$, then

$$\tilde{\beta}(\tilde{\xi}_{\mu}^{\top} \tilde{\mathbf{v}} + \tilde{\mathbf{b}}) = \beta(\xi_{\mu}^{\top} \mathbf{v} + \mathbf{b}) \quad (71)$$

so the softmax outputs f and the system's attractors are unchanged. The visible ODE $\tau_v \dot{\mathbf{v}} = \xi^{\top} f(\mathbf{v}) - \mathbf{v}$ is preserved up to units, as the κ terms can be absorbed into the gain of U2 and U3 without affecting the convergence time bounds.

G Scaling of energy consumption

The energy consumption of DenseAM circuits can be broken up into two parts: the energy dissipated by the weights as a result of Ohm's Law, and the energy from engineering overhead found in amplifiers and active circuitry. The energy dissipated by the weights in the crossbar array can be expressed as the integral of the power dissipated by each resistor of resistance $R_{\mu i}$ from time 0 until convergence at T_{conv} .

Energy consumption of weights. Let the neuron output voltages be proportional to activations: $u_i = \kappa g_i$ and $w_\mu = \kappa f_\mu$, where κ is a fixed voltage scale. We assume rail-bounded outputs $|u_i| \leq \kappa$ and $|w_\mu| \leq \kappa$ (by Appendix F, global rescaling of ξ , voltages, and β preserves the DenseAM dynamics, so this choice of κ does not affect behavior.) The instantaneous power in the resistive crossbar is:

$$P_{\text{weights}}(t) = \sum_{i,\mu} \xi_{\mu i} (u_i - w_\mu)^2 \quad (72)$$

Using the row/column conductance budgets $\sum_\mu \xi_{\mu i} \leq C_c$ and $\sum_i \xi_{\mu i} \leq C_r$ (Appendix E) and the inequality $(a - b)^2 \leq 2a^2 + 2b^2$,

$$P_{\text{weights}}(t) \leq 2 \left(\sum_{i,\mu} \xi_{\mu i} u_i^2 + \sum_{i,\mu} \xi_{\mu i} w_\mu^2 \right) \quad (73)$$

$$= 2 \left(\sum_i u_i^2 \left(\sum_\mu \xi_{\mu i} \right) + \sum_\mu w_\mu^2 \left(\sum_i \xi_{\mu i} \right) \right) \quad (74)$$

$$\leq 2 \left(C_c \sum_i u_i^2 + C_r \sum_\mu w_\mu^2 \right) \quad (75)$$

If the hidden layer uses a softmax activation, then $\sum_\mu f_\mu^2 \leq 1$ and so $\sum_\mu w_\mu^2 \leq \kappa^2$; and rail bounds give $\sum_i u_i^2 \leq N_v \kappa^2$. Therefore,

$$P_{\text{weights}}(t) \leq 2\kappa^2(C_c N_v + C_r) = \mathcal{O}(N_v) \quad (76)$$

Therefore, a system taking time T^{conv} to converge results in an energy consumption of

$$E_{\text{weights}} = \int_0^T P_{\text{weights}}(t) dt \leq 2\kappa^2(C_c N_v + C_r) T^{\text{conv}} \quad (77)$$

According to the convergence time bounds of Appendix E, $T^{\text{conv}} = \mathcal{O}(\tau_v)$. Thus, $E_{\text{weights}} = \mathcal{O}(N_v)$, as a function of system size.

Energy consumption of capacitors. Let each neuron node voltage be bounded by hardware limits $|u_i(t)|, |w_\mu(t)| \leq \kappa$. Charging a capacitor of capacitance C from a supply through a resistive path draws CV^2 from the power supply. The number of times each capacitor charges is finite because the Lyapunov energy of the DenseAM forbids limit cycles. This means the total supply energy per node can be bounded by a constant. Therefore, the total energy needed to (re)charge all neuron capacitors is bounded by

$$E_{\text{capacitors}} \leq \mathcal{O}(1) \cdot \kappa^2 \left(\sum_{i=1}^{N_v} C_i^{(v)} + \sum_{\mu=1}^{N_h} C_\mu^{(h)} \right) = \mathcal{O}(N_v + N_h) \quad (78)$$

Energy consumption of amplifiers, bias, control, and overhead. Per neuron, the energy expenditure to amplifier inefficiency, bias terms, and general overhead do not depend on system size. For a runtime of duration T^{conv} , the energy consumption of these elements in the entire network scales as

$$E_{\text{other}} = \mathcal{O}((N_v + N_h) T^{\text{conv}}) \quad (79)$$

Combined energy consumption. All together, the total energy consumption can be written as

$$E_{\text{total}} = \mathcal{O}(N_v + N_h) \quad (80)$$

H Model Specifications and Details

Table 3, Table 4, and Table 5 summarize the model design for the XOR, Hamming (7,4), and parity DenseAM models.

Table 3: XOR model specification

Visible neurons v_i	$N_v = 3$ (inputs v_1, v_2 clamped to $\{0,1\}$; output v_3 free)
Hidden neurons h_μ	$N_h = 4$ (one per truth-table row)
Visible activation and Lagrangian	Identity: $g_i = v_i$, $\mathcal{L}_v = \frac{1}{2} \sum_{i=1}^{N_v} v_i^2$
Hidden activation and Lagrangian	Softmax: $f_\mu = \text{softmax}(\beta h_\mu)$, $\mathcal{L}_h = \frac{1}{\beta} \log \left(\sum_{\mu=1}^{N_h} e^{\beta h_\mu} \right)$
Visible biases	$a_i = 0$
Hidden biases	$b_\mu = -\frac{1}{2} \sum_{i=1}^{N_v} \xi_{\mu i}^2$
Weights ξ	$\xi \in \{0, 1\}^{4 \times 3}$, rows encode memories: $\xi = \begin{bmatrix} 0 & 0 & 0 \\ 0 & 1 & 1 \\ 1 & 0 & 1 \\ 1 & 1 & 0 \end{bmatrix}$
Inference protocol	Clamp (v_1, v_2) to input values; read out v_3 at convergence

Table 4: Hamming (7,4) model specification

Visible neurons (N_v)	7 (codeword bits)
Hidden neurons (N_h)	16 (one per valid codeword)
Visible activation	Identity: $g_i = v_i$
Hidden activation	Softmax over $\mu \in \{1, \dots, 16\}$ with temperature β
Visible biases	$a_i = 0$
Hidden biases	$b_\mu = -\frac{1}{2} \sum_{i=1}^{N_v} \xi_{\mu i}^2$
Weights ξ	$\xi \in \{0, 1\}^{16 \times 7}$, each row is a valid Hamming(7,4) codeword
Inference protocol	Initialize visible neurons to corrupted 7-bit input codeword; let all visible and hidden neurons evolve; converged visible neurons give the corrected codeword

Table 5: 8-bit parity model specification

Visible neurons v_i	$N_v = 16$ (dimension of embedding D)
Hidden neurons (energy attention) h_A^{attn}	$N_h^{\text{attn}} = 8$ (context length L)
Hidden neurons (Hopfield network) h_μ^{hopf}	$N_h^{\text{hopf}} = 16$ (Hopfield network memories M)
Hidden neurons (total)	$N_h = 24$ ($L + M$)
Visible activation	Identity: $g_i = v_i$
Hidden activation (energy attention)	Softmax: $f_A^{\text{attn}} = \text{softmax}(\beta \mathbf{h}^{\text{attn}})_A$ for $A = 1, \dots, L$
Hidden activation (Hopfield network)	ReLU: $f_\mu^{\text{hopf}} = \max(h_\mu^{\text{hopf}}, 0)$ for $\mu = 1, \dots, M$
Weights (energy attention)	$\xi^{\text{attn}} \in \mathbb{R}^{L \times D}$, where ξ_A^{attn} is embedded A 'th context token
Weights (Hopfield network)	$\xi^{\text{hopf}} \in \mathbb{R}^{M \times D}$, static after training
Inference protocol	Embed L context tokens to obtain ξ^{attn} . Let visible neurons evolve until convergence

H.1 Bit string energy transformer implementation

As described in Table 5, our trained model uses an embedding matrix of $2 \times D = 32$ parameters, the Hopfield network with $D \times M = 256$ parameters, an additional $D \times 2 = 32$ parameter matrix to decode embeddings to logits, a total of $D + L + M = 40$ neuron bias terms, and 2 biases for the linear decoder. This is a total of 362 parameters.

In training and inference we use time constants $\tau_v = 0.1$ and $\tau_h = 0.01$. We train with Euler steps of 1e-3, and test with Euler steps of 1e-4 for a time horizon of $T = 1$ second. Jax’s automatic differentiation was used to implement backpropagation through time. We encourage the model to reach fixed points by penalizing \dot{v} at time T . This yields models that are more robust to hardware imperfection due to the intrinsic stability of attractor points. The convergence to an attractor also means the inference remains stable to mismatch and delay in timing during readout.

I Hardware analysis

I.1 Hardware speed analysis

As discussed in subsection 7.1, the convergence time of analog DenseAMs is governed not by system size, but rather primarily by the timescales of the dynamics in hardware. These timescales are set by the time constants τ_v and τ_h . The smaller these time constants, the faster the dynamics move, and the faster the system converges. In this section, we derive bounds on the minimum time constant $\min\{\tau_v, \tau_h\}$ of the DenseAM, which is limited by the constraints of active components like amplifiers.

The maximum speed of neuronal dynamics is limited by the ability of active stages (op-amps/buffers) to track changing signals. If the input slope to an active stage exceeds its slew rate (SR), the output distorts; if the signal spectrum approaches or exceeds the stage’s closed-loop bandwidth, attenuation and phase lag appear. Here, we derive lower bounds on the time constants τ_v, τ_h imposed by (i) finite gain-bandwidth product (GBW) and (ii) finite SR of the three active stages in the neuron design (Appendix A). Without loss of generality we will express the derivation for the hidden neurons, with the derivations for visible neurons following by symmetry. Throughout, define the following:

- State swing: $|v_i(t)| \leq A_v$, so that $|\dot{v}_i| \lesssim A_v/\tau$. Similarly, $|h_\mu(t)| \leq A_h$, so that $|\dot{h}_\mu| \lesssim A_h/\tau$.
- Activation swing: Visible activation $g(\cdot)$ is Lipschitz with slope bound $L_g = \sup_x |g'(x)|$. Then, $|\dot{g}_i| \leq L_g |\dot{v}_i| \leq L_g A_v/\tau$. Similarly, hidden activation $f(\cdot)$ is Lipschitz with slope bounded by $L_f = \sup_x |f'(x)|$. Then, $|\dot{f}_\mu| \leq L_f |\dot{h}_\mu| \leq L_f A_h/\tau$.
- Weights $\xi \geq 0$. Hardware normalization gives per-row/column conductivity budgets, so the self-term gain for hidden neuron μ is $A_{\text{self},\mu} = \sum_i \xi_{\mu i} = \mathcal{O}(1)$.

We will derive three independent lower bounds and then take the max:

$$\tau_{\min} \geq \max \left\{ \underbrace{\tau_{\text{GBW}}}_{\substack{\text{tracking small signals} \\ \text{edge/large-signals}}}, \underbrace{\tau_{\text{SR}}}_{\text{output current}}, \underbrace{\tau_{I-\text{limit}}}_{\text{}} \right\} \quad (81)$$

I.1.1 Gain-bandwidth product bound

For a single-pole op-amp with gain-bandwidth product GBW in a closed-loop configuration with loop gain A_{CL} , the -3db bandwidth is $f_c \approx \text{GBW}/A_{\text{CL}}$. In order for the neuron to faithfully track with a time constant τ , we require $f_c \gtrsim 1/(2\pi\tau)$ for every stage in the signal path. Closed-loop gains for each of the op-amps are: $A_{\text{CL}}(U1) = 1$ because it is a unity-gain buffer, $A_{\text{CL}}(U2) = A_{\text{self}}$ because it needs to realize the self term gain, and $A_{\text{CL}}(U3) \approx 1$ because it is a unity-gain summer. Assuming the same op-amp design for U1, U2, and U3, and taking the worst case,

$$\tau_{\text{GBW}} = \frac{\max(1, A_{\text{self}})}{2\pi \text{GBW}} \quad (82)$$

I.1.2 Slew rate bound

The slew-rate limits cap the maximum output slope of each op-amp stage:

- **U1: activation buffer.** $|\dot{f}_\mu| \leq L_f A_h/\tau$, which gives $\tau \geq (L_f A_h)/\text{SR}_{U1}$.

Table 6: Estimated neuron time constants and conservative convergence times with $A_v = A_h = 1\text{ V}$, $L_g = 1$, $A_{\text{self}} = 1$ for representative amplifiers in literature. GBW bound $\tau_{\text{GBW}} = \frac{1}{2\pi \text{GBW}}$; SR bound $\tau_{\text{SR}} = \frac{L_g A_v}{\text{SR}}$ (visible path). Overall $\tau_{\text{min}} = \max\{\tau_{\text{GBW}}, \tau_{\text{SR}}\}$; we report $T_{\text{conv}} = 10 \tau_{\text{min}}$.

CMOS Amplifier (ref.)	SR (V/ μs)	GBW (MHz)	τ_{SR} (ns)	τ_{GBW} (ns)	T_{conv} (ns)
Perez and Maloberti [36]	84.50	321.50	11.83	0.50	118.34
Assaad and Silva-Martinez [37]	94.10	134.20	10.63	1.19	106.27
Yen and Blalock [38]	202.00	10.70	4.95	14.87	148.74
Naderi, Prakash, and Silva-Martinez [39]	1250.00	3600.00	0.80	0.04	8.00
Schlögl and Zimmermann [40]	1650.00	2510.00	0.61	0.06	6.06

Notes. (i) τ_{SR} values assume the visible path dominates the summer's SR (low/moderate- β). If softmax dominates at U3 in the high- β regime, multiply SR-limited values by $\kappa = (\beta/2)(A_h/A_v)$ (with $A_h = A_v = 1\text{ V}$, simply $\beta/2$). (ii) The current-limit bound $\tau_{\text{I-limit}} = CA_v/I_{\text{max}}$ is typically \ll all reported values for $C \sim 50\text{ fF}$ and $I_{\text{max}} \sim \text{mA}$, so it is omitted from the table but must still be respected in circuit sizing.

- **U2: self-term.** $s_\mu = A_{\text{self}} f_\mu$, so $|\dot{s}_\mu| = A_{\text{self}} |\dot{f}_\mu| \leq (A_{\text{self}} L_f A_h)/\tau$, which gives $\tau \geq (A_{\text{self}} L_f A_h)/\text{SR}_{\text{U2}}$.
- **U3: internal state drive.** The time-varying portion of the RC circuit drive d_μ is a linear combination of f_μ and g_i , with coefficients that have a maximum magnitude of A_{self} . Using the bounds on the slopes of those inputs, we get the following bound on $|\dot{d}_\mu|$ and subsequently the time constant bound:

$$|\dot{d}_\mu| \lesssim \frac{A_{\text{self}}}{\tau} \max\{L_f A_h, L_g A_v\} \Rightarrow \tau \geq \frac{A_{\text{self}} \max(L_f A_h, L_g A_v)}{\text{SR}_{\text{U3}}} \quad (83)$$

All together, the combined constraint is

$$\tau_{\text{SR}} = \max \left\{ \frac{L_f A_h}{\text{SR}_{\text{U1}}}, \frac{A_{\text{self}} L_f A_h}{\text{SR}_{\text{U2}}}, \frac{A_{\text{self}} \max(L_f A_h, L_g A_v)}{\text{SR}_{\text{U3}}} \right\} \quad (84)$$

I.1.3 Current / headroom limit

U3 must provide the current through R_2 to charge C_1 . The RC circuit dynamics dictate $R_2 C_1 \dot{h}_\mu = -h_\mu + d_\mu$, so the instantaneous current needed by U3 is

$$I_{\text{U3,out}} = \frac{d_\mu - h_\mu}{R_2} = C_1 \dot{h}_\mu \quad (85)$$

We must respect $|I_{\text{U3,out}}| \leq I_{\text{max,U3}}$. With $|\dot{h}_\mu| \lesssim A_h/\tau$,

$$\tau_{\text{I-limit}} \geq \frac{C_1 A_h}{I_{\text{max,U3}}} \quad (86)$$

I.1.4 Combined bound on minimum time constant

Taken together, the minimum time constant must satisfy the bounds (82), (84), and (86):

$$\tau_{\text{min}} \geq \max\{\tau_{\text{GBW}}, \tau_{\text{SR}}, \tau_{\text{I-limit}}\} \quad (87)$$

I.2 Estimates of inference times with existing hardware

Under standard assumptions for DenseAMs (symmetric couplings and monotone activations), the Lyapunov energy decreases monotonically and the dynamics converge without oscillations. The settling time is therefore on the order of a few multiples of the largest neuronal time constant, which we bound by amplifier non-idealities. In this section we take some representative examples of op-amps from literature and estimate the inference speeds from reasonable and representative design parameters.

Minimum time constant. For illustration purposes, we choose three reasonable hardware constraints:

- **Activation slopes.** Take the slope of the visible activation to be $L_g = 1$, such as would occur in a identity visible neuron activation. Take the worst-case (maximum) slope of the hidden activation to be according to the softmax with fixed β , whose Jacobian is $\beta G(\mathbf{f})$ with $\|G(\mathbf{f})\|_2 \leq \frac{1}{2}$, so a safe global bound is $L_f \leq \frac{\beta}{2}$.
- **Signal swing.** Use the voltage scaling invariance (see Appendix F) to rescale \mathbf{v} , $\boldsymbol{\xi}$, and β together to pick a swing that is slew-rate friendly but well above component noise limits. Take both $A_v = A_h = 1V$.
- **Self-term gain.** With row/column budgets, use A_{self} as a worst-case bound.

With those choices, the three lower bounds per neuron are:

1. **GBW Bound:** $\tau_{\text{GBW}} = \frac{\max(1, A_{\text{self}})}{2\pi \text{GBW}} = \frac{1}{2\pi \text{GBW}}$.
2. **SR Bound:** The U1/U2 path give $\tau_{\text{SR,vis}} = \frac{L_g A_v}{\text{SR}} = \frac{1}{\text{SR}} \mu\text{s}$. In the U3 (summer) path, equation (84) has two cases. In the low- β regime where $L_g A_v \geq L_f A_h$, then U3 bound reduces to $1/\text{SR} \mu\text{s}$. In the high- β regime where $L_f A_h = \beta/2$ dominates, scale the slew-rate limited bound by $\beta/2$.
3. **Output Current Bound:** In practice, this bound generally does not limit the op amp choice: even with a large capacitor $C = 50 \text{ fF}$, $A_v = 1V$, $I_{\text{max}} = 2\text{mA}$, $\tau_{\text{I-limit}} \approx 0.025\text{ns}$, which is negligible compared to the bounds from SR and GBW.

To quantify realistic inference speeds, Table 6 lists representative CMOS operational transconductance amplifiers (OTAs)³ drawn from recent literature, together with their corresponding lower bounds on neuronal time constants under the GBW and slew-rate limits. Even using conservative assumptions with existing amplifier designs, the analysis shows that modern high-speed OTAs can achieve sub-10 ns neuronal convergence times—corresponding to inference rates in the hundreds of megahertz.

J Connection between analog and canonical Energy Transformer

In this section we show that in the adiabatic limit, our Analog Energy Transformer (Analog ET) reduces to the canonical Energy Transformer. Begin with the dynamics for the Analog Energy Transformer implemented by our circuit designs.

$$\tau_v \dot{\mathbf{v}} = -\frac{\partial E}{\partial \mathbf{v}} = (\boldsymbol{\xi}^{\text{attn}})^\top \mathbf{f}^{\text{attn}} + (\boldsymbol{\xi}^{\text{hopf}})^\top \mathbf{f}^{\text{hopf}} + \mathbf{a} - \mathbf{v} \quad (88)$$

$$\tau_h \dot{\mathbf{h}}^{\text{attn}} = -\frac{\partial E}{\partial \mathbf{f}^{\text{attn}}} = \boldsymbol{\xi}^{\text{attn}} \mathbf{v} + \mathbf{b} - \mathbf{h}^{\text{attn}} \quad (89)$$

$$\tau_h \dot{\mathbf{h}}^{\text{hopf}} = -\frac{\partial E}{\partial \mathbf{f}^{\text{hopf}}} = \boldsymbol{\xi}^{\text{hopf}} \mathbf{v} + \mathbf{c} - \mathbf{h}^{\text{hopf}} \quad (90)$$

Integrating out hidden neurons in the adiabatic limit where $\tau_h \rightarrow 0$, we see the relations

$$\mathbf{h}^{\text{attn}}(\mathbf{v}) = \boldsymbol{\xi}^{\text{attn}} \mathbf{v} + \mathbf{b} \quad (91)$$

$$\mathbf{h}^{\text{hopf}}(\mathbf{v}) = \boldsymbol{\xi}^{\text{hopf}} \mathbf{v} + \mathbf{c} \quad (92)$$

which we can use to integrate out the hidden neuron activations as

$$\mathbf{f}^{\text{attn}}(\mathbf{v}) = \text{softmax}(\boldsymbol{\xi}^{\text{attn}} \mathbf{v} + \mathbf{b}) \quad (93)$$

$$\mathbf{f}^{\text{hopf}}(\mathbf{v}) = \text{ReLU}(\boldsymbol{\xi}^{\text{hopf}} \mathbf{v} + \mathbf{c}) \quad (94)$$

Substituting into the visible dynamics:

$$\tau_v \dot{\mathbf{v}} = (\boldsymbol{\xi}^{\text{attn}})^\top \mathbf{f}^{\text{attn}}(\mathbf{v}) + (\boldsymbol{\xi}^{\text{hopf}})^\top \mathbf{f}^{\text{hopf}}(\mathbf{v}) + \mathbf{a} - \mathbf{v} \quad (95)$$

³Many high-speed CMOS “op-amps” are reported as OTAs (transconductors). In our neuron, these OTA cores operate in closed-loop (unity/non-inverting) configurations, so the literature SR and GBW directly constrain τ via Eqs. (82)–(84).

We can ask ourselves, what scalar energy produces this ODE? We seek an energy $E_{\text{eff}}(\mathbf{v})$ such that $\tau_v \dot{\mathbf{v}} = -\frac{\partial E_{\text{eff}}}{\partial \mathbf{v}}$. Equivalently,

$$\nabla_{\mathbf{v}} E_{\text{eff}}(\mathbf{v}) = \mathbf{v} - \mathbf{a} - (\boldsymbol{\xi}^{\text{attn}})^{\top} \mathbf{f}^{\text{attn}}(\mathbf{v}) - (\boldsymbol{\xi}^{\text{hopf}})^{\top} \mathbf{f}^{\text{hopf}}(\mathbf{v}) \quad (96)$$

We can construct $E_{\text{eff}}(\mathbf{v})$ as a sum of three pieces whose gradients match each term $E_{\text{eff}}(\mathbf{v}) = E_{\text{quad}}(\mathbf{v}) + E_{\text{attn}}(\mathbf{v}) + E_{\text{hopf}}(\mathbf{v})$. By inspection we see that $E_{\text{quad}}(\mathbf{v}) = \frac{1}{2} \|\mathbf{v} - \mathbf{a}\|^2$.

Attention term. The energy function

$$E_{\text{attn}}(\mathbf{v}) = -\frac{1}{\beta} \log \sum_A \exp(\beta (\boldsymbol{\xi}_A^{\text{attn}} \mathbf{v} + b_A)) \quad (97)$$

satisfies our requirement. We can see that by differentiating with respect to v_i , we get

$$\frac{\partial E_{\text{attn}}}{\partial v_i} = -\sum_A \text{softmax}(\boldsymbol{\xi}^{\text{attn}} \mathbf{v} + \mathbf{b})_A \cdot \boldsymbol{\xi}_{Ai}^{\text{attn}} \quad (98)$$

$$= -\sum_A \boldsymbol{\xi}_{Ai}^{\text{attn}} f_A^{\text{attn}}(\mathbf{v}) \quad (99)$$

which yields our desired dynamics of $\nabla_{\mathbf{v}} E_{\text{attn}}(\mathbf{v}) = -(\boldsymbol{\xi}^{\text{attn}})^{\top} \mathbf{f}^{\text{attn}}(\mathbf{v})$.

Hopfield term. A simple way to achieve the desired dynamics is with a Hopfield-type energy function

$$E_{\text{hopf}}(\mathbf{v}) = -\sum_{\mu} \frac{1}{2} \left(\text{ReLU}(\boldsymbol{\xi}_{\mu}^{\text{hopf}} \mathbf{v} + c_{\mu}) \right)^2 \quad (100)$$

whose derivative with respect to v_i yields

$$\frac{\partial E_{\text{hopf}}}{\partial v_i} = -\sum_{\mu} \text{ReLU}(\boldsymbol{\xi}_{\mu}^{\text{hopf}} \mathbf{v} + c_{\mu}) \cdot \boldsymbol{\xi}_{\mu i}^{\text{hopf}} \quad (101)$$

$$= -\sum_{\mu} \boldsymbol{\xi}_{\mu i}^{\text{hopf}} f_{\mu}^{\text{hopf}}(\mathbf{v}) \quad (102)$$

which yields our desired dynamics of $\nabla_{\mathbf{v}} E_{\text{hopf}}(\mathbf{v}) = -(\boldsymbol{\xi}^{\text{hopf}})^{\top} \mathbf{f}^{\text{hopf}}(\mathbf{v})$.

Effective energy function of analog energy transformer. All together, the effective scalar energy over the visible state \mathbf{v} after integrating out hidden neurons is

$$E_{\text{eff}}(\mathbf{v}) = \underbrace{\frac{1}{2} \|\mathbf{v} - \mathbf{a}\|_2^2}_{E_{\text{quad}}} - \underbrace{\frac{1}{\beta} \log \sum_A \exp(\beta (\boldsymbol{\xi}_A^{\text{attn}} \mathbf{v} + b_A))}_{E_{\text{attn}}} - \underbrace{\sum_{\mu} \frac{1}{2} \left(\text{ReLU}(\boldsymbol{\xi}_{\mu}^{\text{hopf}} \mathbf{v} + c_{\mu}) \right)^2}_{E_{\text{hopf}}} \quad (103)$$

This effective energy aligns with the canonical Energy Transformer's energy function. Because our effective dynamics use hidden neurons, the energy function written in the main text reflects the contributions of the hidden neurons. When $\tau_h \ll \tau_v$, this regime converges to the behavior when the hidden neurons are integrated out. Hence, the effective expressibility and behavior of our system is equivalent to that of the original Energy Transformer.

In our model we omit the layer normalization activation that the original Energy Transformer applies to the visible neurons. This keeps the circuit design simple, while still enabling models with high expressibility. This choice does not modify the structure of the attention or the Hopfield parts of the energy; only the self-energy of \mathbf{v} differs. From a modeling perspective, layer normalization mainly improves conditioning and learning of deep networks rather than changing the computational primitive and expressibility. We empirically observe that the resulting models without layer normalization remain expressive enough to solve the problems we present. In principle, a layer normalization-type visible activation function could be implemented in analog hardware (e.g. by subtracting the mean voltage and normalizing by an on-chip variance estimate), but this would add distracting complications to the minimalist neuron and circuit designs we show in this paper.